

5-2019

Mathematical Model Investigating the Effects of Neurostimulation Therapies on Neural Functioning: Comparing the Effects of Neuromodulation Techniques on Ion Channel Gating and Ionic Flux Using Finite Element Analysis

Kaia Lindberg

Follow this and additional works at: https://docs.rwu.edu/math_theses

Part of the [Applied Mathematics Commons](#)

*Mathematical Model Investigating the Effects of
Neurostimulation Therapies on Neural Functioning:
Comparing the Effects of Neuromodulation Techniques on
Ion Channel Gating and Ionic Flux Using Finite Element
Analysis*

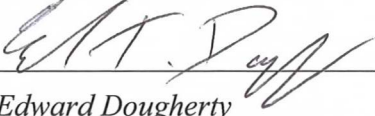
Kaia Lindberg

*Bachelor of Science
Mathematics*

Feinstein College of Arts and Sciences
Roger Williams University

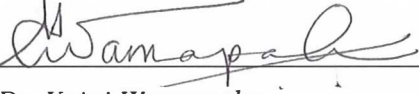
May 2019

The thesis of Kaia Lindberg was reviewed by and approved by the following:




Dr. Edward Dougherty
Professor of Mathematics
Thesis Advisor

Date: 4/17/2019



Dr. Yajni Warnapala
Department Chair, Professor of Mathematics

Date: 4/17/19



Dr. Victoria Heimer-McGinn
Professor of Psychology

Date: 4/17/2019

Acknowledgements

Thank you to Dr. Edward Dougherty. Without his dedicated guidance, instruction, and advice throughout the past two years of working on this project this thesis would not have been possible. In addition, thank you to the past and present members of our research team: Abigail Small, Elizabeth Gilchrist, Madison Guitard, and Andrew Delsanto.

Thank you to Dr. Yajni Warnapala and Dr. Victoria Heimer-McGinn for being on the committee for this thesis and for their feedback that helped strengthen this research and thesis. This research was supported by the Summer Undergraduate Research Fellowship (SURF) Program of the Rhode Island Institutional Development Award (IDeA) Network for Biomedical Research Excellence from the National Institute of General Medical Sciences of the National Institutes of Health under grant number P20GM103430. Finally, thank you to the Roger Williams University Provost's Fund, Student Senate Academic Allocations Committee, and Joint Mathematics Meeting Student Travel Grant for providing funding for the opportunity to present this research at local, regional, and national conferences.

I dedicate this thesis to my family for their endless support and encouragement.

Contents

1	Introduction	1
2	Methods and Procedures	4
2.1	Poisson-Nernst-Planck Model	4
2.2	Computational Domain	5
2.3	Boundary Conditions	6
2.3.1	DBS and TES Boundary Conditions	7
2.3.2	Transmembrane Flux Boundary Conditions	8
2.3.3	Additional Boundary Conditions	10
2.4	Numerical Implementation	10
2.5	PDE Weak Formulation Derivations	11
2.5.1	Poisson Equation	11
2.5.2	Nernst-Planck Equation	12
2.6	Computational Tools	13
2.7	Numerical Simulations	14
3	Transcranial Electrical Stimulation Results	16
3.1	Transmembrane Voltage Polarization Exhibits Location Specificity	16
3.2	Voltage Gated Ion Channel State Variables Exhibit Location Specificity	18
3.3	Membrane Ion Flux Exhibits Location Specificity	20
3.4	TES Causes Intracellular Calcium Dyshomeostasis	21
4	Deep Brain Stimulation and Comparison Results	22
4.1	Instantaneous Transmembrane Polarization	22
4.2	Asymmetric Location Specificity in Ion Channel Gating Variables	26
4.3	Speed of Changes in Gating Variables	29
4.4	Transmembrane Ionic Flux	30
5	Discussion	34
5.1	Future Directions	36
A	Mathematical Concepts and Definitions	43
A.1	Finite Element Method	43
A.1.1	Function Spaces	44
A.1.2	Finite Element Method Steps	45
A.1.3	One Dimensional Example	46
A.2	Gauss-Seidel Method	47

List of Figures

1	Diagram illustrating the structure of a neuron within the brain, especially the node of Ranvier region	5
2	Diagram of computational domain with intracellular (Ω_I), membrane (Ω_M), and extracellular (Ω_E) subdomains	6
3	Computational mesh with nodes on which the PDEs are solved	7
4	Diagram illustrating the object-oriented approach to the software's design with the relationships between the different classes	14
5	Electric potential energy (ϕ) throughout the computational domain during TES treatment	16
6	Transmembrane voltage during TES treatment	17
7	Gating variable values due to TES application at equispaced locations within the node of Ranvier	18
8	Gating variable values during TES at each location along the node of Ranvier at simulation times $t = 2.0, 2.1, 2.2, 2.5, 5, 10,$ and 20 ms	20
9	Transmembrane ionic flux due to the application of a TES stimulus	20
10	Concentration of calcium in the intracellular space during the simulation at times $t = 0, 2, 5, 10, 15,$ and 20 ms	22
11	Comparison of electric potential energy throughout the domain	23
12	Transmembrane voltage during DBS and TES treatment	24
13	Gating variables at equispaced positions along the node of Ranvier during DBS treatment	26
14	Comparison of changes in gating variables between DBS and TES	28
15	Transmembrane ionic flux during DBS and TES simulations	31
16	Electric potential energy throughout a computational domain of a neuron with three nodes of Ranvier	36
17	Extracellular concentration of calcium during TES in a three-dimensional computational domain	36
18	Illustration of finite element approximation of a one-dimensional problem	47

List of Tables

1	Parameters for the PNP model of electrodiffusion	5
2	Ion channel conductance parameters used in the calculation of membrane current for each ion	10
3	Neurostimulation treatment (stimulus amplitude, frequency, and duration) and simulation (time step, simulation length) parameters	15
4	Asymmetry in changes in DBS gating variables	28
5	Changes in transmembrane flux during neurostimulation treatments	33

Abstract

Neurostimulation therapies demonstrate success as a medical intervention for individuals with neurodegenerative diseases, such as Parkinson's and Alzheimer's disease. Despite promising results from these treatments, the influence of an electric current on ion concentrations and subsequent transmembrane voltage is unclear. This project focuses on developing a unique cellular-level mathematical model of neurostimulation to better understand its effects on neuronal electrodynamics. The mathematical model presented here integrates the Poisson-Nernst-Planck system of PDEs and Hodgkin-Huxley based ODEs to model the effects of this neurotherapy on transmembrane voltage, ion channel gating, and ionic mobility. This system is decoupled using the Gauss-Seidel method and then the equations are solved using the finite element method on a biologically-inspired discretized domain. Results demonstrate the influence of transcranial electrical stimulation on membrane voltage, ion channel gating, and transmembrane flux. Simulations also compare the effects of two different types of neurostimulation (transcranial electrical stimulation and deep brain stimulation) showcasing cellular-level differences resulting from these distinct forms of electrical therapy. Hopefully this work will ultimately help elucidate the principles by which neurostimulation alleviates disease symptoms.

1 Introduction

Clinical experiments have demonstrated the efficacy of neuromodulation techniques in treating a variety of neurological conditions including Parkinson’s disease (PD) and Alzheimer’s disease [1–4]. There are several types of neurostimulation currently used for the treatment of neurodegenerative diseases, including transcranial electrical stimulation (TES) and deep brain stimulation (DBS).

Transcranial electrical stimulation (TES) is a group of neurostimulation therapies that deliver low doses of electric current to targeted brain regions via noninvasive electrodes placed on a patient’s scalp. The most common type of TES is transcranial direct current stimulation (tDCS), which administers a constant amount of electrical energy during therapy sessions. Other forms of TES include transcranial alternating current stimulation (tACS) as well as transcranial random noise stimulation (tRNS), both of which utilize a non-constant dosage of electric current [5,6]. Most recently, high-definition TES has been introduced as a neurostimulation approach that achieves a more focused delivery of electrical energy through the use of numerous smaller anode and cathode electrodes, as opposed to just the single larger-sized anode and cathode traditionally used in tDCS, tACS, and tRNS [7,8]. On the other hand, deep brain stimulation is a more invasive treatment that involves surgically implanting electrodes, which deliver stimuli directly to targeted regions of the brain via a pacemaker typically placed just below the clavicle [9,10].

Clinical experiments clearly show that TES is an effective intervention for treating conditions that manifest from neurodegenerative disorders. Parkinson’s disease patients, for example, have demonstrated enhanced movement capabilities and memory skills from TES [2,11]. Also, individuals suffering from Alzheimer’s disease have demonstrated improved recognition and memory capabilities [3,4]. Further, TES has shown to improve language re-learning in dementia patients [12,13]. Recently, TES has shown to alleviate numerous psychological symptoms that manifest from post-traumatic stress disorder [14–16]. In contrast, DBS has historically been restricted to treating movement disorders, and has shown to be effective in improving symptoms for patients with PD, essential tremor [17–19], and dystonia [20,21]. More recently, DBS has demonstrated success in alleviating symptoms of psychiatric disorders such as obsessive compulsive disorder and major depressive disorder [22–24].

In addition to clinical findings, biological experiments have begun to show the effects of TES and DBS on membrane polarization [25–28] and calcium homeostasis [29–31], however difficulties in capturing ion channel state, ionic flux, and intracellular calcium concentrations continuously over time with a high sampling frequency yields limited neurostimulation data at the cellular level [31]. Thus, the direct influence of an applied electric current on voltage-gated ion channel states as well as other cellular level mechanism by which neurostimulation operates is largely unknown [32].

As an accompaniment to biomedical experimentation, mathematical modeling and computational simulation are helping to address this knowledge gap by enabling *in silico* investigations of the impact of an applied electrical stimulation on the brain. Computer-based simulations of DBS have investigated the effect of changing electrode parameters including electrode size, shape, and stimulation settings on the electric field distribution and neural excitation [33–36]. Other research has coupled models of the electric field in the extracellular space with multi-compartment cable models of neurons to demonstrate the effects of DBS on neural activity and predict action potential generation. These simulations show both depolarizing and hyper-polarizing effects in the neuron as well as activation and suppression of action potential generation, depending on the neuron’s position and orientation in relation to the electrode [37–39].

Computational simulations have also helped to enhance the neurological communities’ understanding of TES. Recent models have begun to describe the impact of electrical stimulation on electric potential around neural tissue [40]. In addition, biodomain models have provided a means to begin to characterize the influence of electrical energy on transmembrane potential using volume averaging approaches [41, 42]. These models support the physiological conclusion that TES influences the neuron by slightly polarizing the cell membrane [32], however, the level of biological abstraction of their mathematical formulations inherently prohibits a quantitative description of individual ion species and their movements around and through the neuron cell wall.

Despite promising clinical results from both TES and DBS, as well as a basic comprehension of their anatomical extents, the precise mechanisms by which these treatments impact cellular level electrodynamics are still largely unknown. While it is generally accepted that the electric current causes variation in the neuron’s resting membrane potential, the details of this modification remain uncertain. In addition, the effects on ion channel gating,

ionic flux, and individual ion concentrations are unknown. Knowledge of how electrical therapies operate at the cellular level will fundamentally enhance our understanding of neuronal electrophysiology due to neurostimulation treatments, and in doing so, could help uncover potential neurotherapeutic targets for treating the progression of neurological disorders. In addition, investigating differences in neuron response due to DBS and TES would facilitate an even greater understanding of the advantages, limitations, and mechanisms by which these forms of neuromodulation operate to achieve therapeutic success.

To do so we present a novel mathematical model of neurostimulation that provides a description of its effects on cellular level neuronal electrodynamics. The model integrates the Poisson-Nernst-Planck electrodiffusion system of partial differential equations (PDEs) [43, 44] and Hodgkin-Huxley [45] motivated boundary conditions for cell membrane ionic flux with extracellular boundary conditions that model neurostimulation treatments. Four ion species, namely sodium, potassium, chloride, and calcium, are incorporated in the model. We include calcium in this model as cytosolic calcium is known to be an essential member of the intracellular biochemical network that triggers proper neurotransmitter secretion, and in addition, holds an integral connection with neurodegenerative diseases [46–49]. The model is then simulated on a biologically-inspired computational domain [50–52] that includes intracellular, extracellular, and membrane regions. Using *in silico* experiments, we examine the impact of neurostimulation on (i) extracellular and intracellular electric potential, (ii) resting membrane potential along the node of Ranvier, (iii) voltage-dependent ion channel gating, (iv) ionic membrane flux, and (v) extracellular and intracellular ion diffusion.

First, the model is used to simulate TES, a low-dose, non-invasive neurostimulation therapy. Next, the model is adjusted slightly to simulate the higher-intensity and intermittent current applied during DBS. Using the same model to simulate these two neuromodulation techniques (DBS and TES) allows for a comprehensive comparison of the effects of these two treatments on cellular level processes.

To our knowledge, this paper presents the first neurostimulation model that incorporates the effect of these therapies on individual ion concentrations and membrane fluxes as well as the state of voltage gated ion channels at locations along the membrane during treatment. In addition, this research is the first numerical comparison of DBS and TES on cellular level neurophysiological processes. It is our goal that the approaches and simulation results presented here help refine the communities' understanding of neuronal

functioning due to both DBS and TES.

2 Methods and Procedures

2.1 Poisson-Nernst-Planck Model

The time-dependent Poisson-Nernst-Planck (PNP) system of partial differential equations (PDEs) can be used to model ion electrodiffusion around and within a neuron [43, 53].

Electrodiffusion is the process that describes the movement of charged particles (ions) in a medium under the influence of electric potential and an ionic concentration gradient. The Nernst-Planck equation, which describes particle movement due to both diffusion and electrostatic forces, is given by

$$\frac{\partial n_i}{\partial t} + \nabla \cdot F_i = 0, \quad (1)$$

where the ion flux, F_i , is given by

$$F_i = -D_i(\nabla n_i + \frac{n_i}{\alpha_i} \nabla \phi), \quad (2)$$

where $n_i = n_i(\vec{x}, t)$ and $\phi = \phi(\vec{x}, t)$ represent the concentration of the i^{th} ion and the electric potential energy respectively, both of which are unknown quantities to be solved for. In addition, constant D_i is the diffusivity in water for the i^{th} ion and the constant α_i equals $\frac{RT}{Fz_i}$, where R , T , and F are the gas constant, temperature of the medium, and Faraday's constant respectively.

The Poisson equation portion of the PNP system quantifies the electric potential energy due to ion concentrations and their relative valences, and is given by

$$\nabla \cdot (\epsilon \nabla \phi) = -F \sum_{i=1} z_i n_i, \quad (3)$$

where z_i is the valence of ion i . In addition, ϵ denotes the permittivity of the medium, equaling $\epsilon_c \cdot \epsilon_0$ in intracellular and extracellular regions, and $\epsilon_{memb} \cdot \epsilon_0$ in the cell membrane. Here, ϵ_0 is given by vacuum permittivity while ϵ_c and ϵ_{memb} are relative permittivities of the intra/extra-cellular and membrane domains respectively.

In this paper, four ion species are used in the PNP model, namely sodium (Na^+), potassium (K^+), calcium (Ca^{+2}), and chloride (Cl^-); thus, Equation 1 is realized four times,

and the summation term of Equation 3 contains four terms. Values of these parameters as well as initial ion concentrations are given in Table 1.

Table 1: **Parameters for the PNP model of electrodiffusion.**

Parameter	Value
Perfect Gas Constant	$8.31 \text{ J} \cdot \text{mole}^{-1} \cdot \text{K}^{-1}$
Faraday's Constant	$96485 \text{ C} \cdot \text{mole}^{-1}$
Temperature	279.45 K
Vacuum Permittivity	$8.89 \cdot 10^{-12} \text{ C} \cdot \text{m}^{-1} \cdot \text{V}^{-1}$
Cytosol Relative Permittivity	80
Membrane Relative Permittivity	2
Initial Na^+ Intracellular Concentration	12 mM
Initial Na^+ Extracellular Concentration	145 mM
Initial K^+ Intracellular Concentration	155 mM
Initial K^+ Extracellular Concentration	4 mM
Initial Ca^{+2} Intracellular Concentration	0.0001 mM
Initial Ca^{+2} Extracellular Concentration	1 mM
Initial Cl^- Intracellular Concentration	166.8 mM
Initial Cl^- Extracellular Concentration	123.27 mM
Na^+ Diffusivity	$1.33 \cdot 10^{-9} \text{ m}^2 \cdot \text{s}^{-1}$
K^+ Diffusivity	$1.96 \cdot 10^{-9} \text{ m}^2 \cdot \text{s}^{-1}$
Ca^{+2} Diffusivity	$0.5 \cdot 10^{-9} \text{ m}^2 \cdot \text{s}^{-1}$
Cl^- Diffusivity	$2.0 \cdot 10^{-9} \text{ m}^2 \cdot \text{s}^{-1}$

2.2 Computational Domain

The brain contains billions of neurons, which are responsible for transmitting information to other cells. Each neuron consists of a cell body with the nucleus, an axon, and dendrites, as illustrated in Figure 1. Nodes of Ranvier are the regions of the axon that are rich in ion channels and thus play an important role in transmembrane ionic transport.

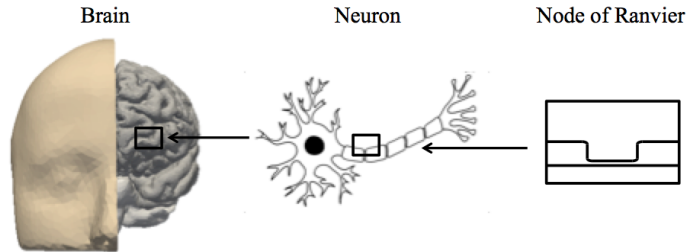


Figure 1: **Diagram illustrating the structure of a neuron within the brain.** The node of Ranvier region is highlighted, which is the region that is modeled in these simulations, is highlighted in this diagram.

The model is simulated on a biologically-inspired two-dimensional domain representing a

portion of a neuron axon that includes a single node of Ranvier. The domain was constructed using both the myelinated and unmyelinated regions of the membrane, and biologically accurate dimensions were incorporated [43, 44, 50–52, 54–57]. The three subregions of the computational domain consists of (i) intracellular space, (ii) membrane, (iii) and extracellular space. Figure 2 presents the domain, noting the locations of the three regions as well as all domain boundaries. The length of the axon portion of the domain is $4\ \mu\text{m}$ [43, 56] with the nodal portion having a length of $1\ \mu\text{m}$ [43, 50, 51, 54, 56]. The radius of the myelinated and unmyelinated sections of the membrane are $0.406\ \mu\text{m}$ [43, 56] and $0.005\ \mu\text{m}$ [44, 52, 55], respectively. The radius of the intracellular space is $0.434\ \mu\text{m}$ [43, 56], and the whole domain, i.e. intracellular, membrane, and extracellular spaces, has a radius of $2\ \mu\text{m}$ [43, 56].

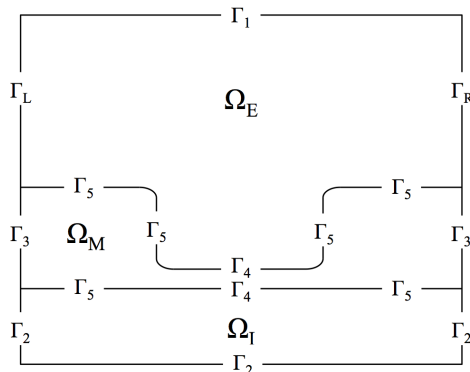


Figure 2: **Diagram of computational domain with intracellular (Ω_I), membrane (Ω_M), and extracellular (Ω_E) subdomains.** The diagram also includes labels for each boundary in the domain. Γ_L and Γ_R are the boundaries for the left and right sides of the extracellular space respectively. Γ_1 is the boundary for the top of the extracellular space and Γ_2 labels the exterior boundaries for the intracellular subdomain. Γ_3 is the exterior boundary of the membrane and Γ_5 labels the boundary between the membrane and intra/extra-cellular space other than in the node of Ranvier, which is labeled by Γ_4 .

Figure 3 displays the discretized computational mesh used in each simulation; in this mesh, there are 725,528 elements, with 67,810 nodes in the membrane, 502,644 in the intracellular space, and 159,410 in the extracellular space. The mesh has a much finer grid resolution in the Debye layer, the extracellular space directly adjacent to the membrane, as well as its neighboring intracellular space; this finer discretization is necessary to accurately model the rapid solution changes that take place in these regions of the domain [44].

2.3 Boundary Conditions

Equation 1 is defined on the intracellular and extracellular regions of the domain, namely $\Omega_I \cup \Omega_E$, whereas Equation 3 is defined on the entire domain $\Omega = \Omega_I \cup \Omega_M \cup \Omega_E$ [44]. Thus,

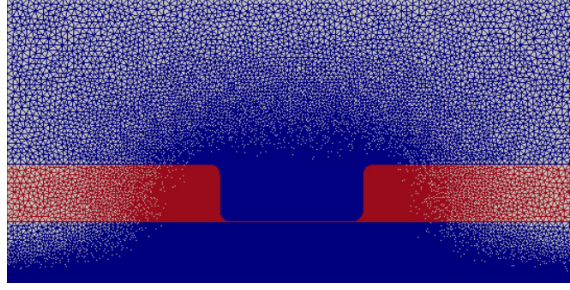


Figure 3: **Computational mesh with nodes on which the PDEs are solved.** Intracellular and extracellular subdomains are shown in blue and the membrane region is shown in red.

boundary conditions for these equations must be stipulated on these respective boundaries. To appropriately model TES at the cellular level, boundary conditions for the Nernst-Planck equation and the Poisson equation must be specified to model TES administration as well as ion transport across the cell membrane. These conditions are described in the following sections.

2.3.1 DBS and TES Boundary Conditions

A fundamental difference between DBS and TES is the waveform of applied electrical stimulation. Constant stimulation TES, typically called transcranial direct current stimulation (tDCS), delivers a low, but constant dose of electric current during treatment. On the contrary, DBS delivers higher doses of electric current at intermittent intervals/pulses. During DBS treatments, the stimulus amplitude is typically between 1 V and 5 V with a pulse duration from 60 μ s to 200 μ s, and a frequency that can range from 120 Hz to 180 Hz [58–60]. For DBS simulations in this paper, all stimulus parameters were chosen to be within these ranges. Specifically, a stimulation amplitude of 3 V is used, with a duration of 100 μ s, and frequency of 150 Hz. Further, all of these values are consistent with prior models of DBS [37, 38].

Prior to treatment, depicting a neuron under normal conditions, the left and right sides of the domain act as the ground with electric potential values of zero. The external current is then applied to the left side of the domain with the right side remaining as the ground.

For both TES and DBS simulations, the electric potential on right side of the extracellular space (Γ_R) is maintained at a value of zero using the homogeneous Dirichlet boundary condition

$$\phi = 0, \quad \vec{x} \in \Gamma_R. \quad (4)$$

Electrical stimulation for both TES and DBS is simulated using a time-dependent Dirichlet boundary condition for the Poisson equation (Equation 3) on the left extracellular space boundary, Γ_L . For TES, the value of the electric potential on Γ_L is set to 0 V for the first 1 ms of the simulation. Then, this value is changed to 0.1 V, effectively simulating the start of the TES therapy. This dosage is consistent with electric potentials achieved within neural tissue during TES sessions [61–63]. This boundary condition is stipulated with the following equation

$$\phi = \begin{cases} 0 : & t \leq 1 \text{ ms}, \vec{x} \in \Gamma_L \\ 0.1 : & t > 1 \text{ ms}, \vec{x} \in \Gamma_L \end{cases} \quad (5)$$

Unlike TES, DBS administers a higher dose of electric current and the application is intermittent, and so a larger and non-constant value of ϕ is used. Like TES, the value of electric potential on Γ_L is set to 0 V for the first 1 ms of the DBS simulation, and after this time, DBS treatment begins by changing ϕ on Γ_L to 3 V. This value is maintained for 0.1 ms, at which time the stimulation is returned to zero for 6.5 ms, based on a frequency of 150 Hz. Two additional pulses are applied with the same amplitude, pulse width, and frequency. This complete DBS waveform is governed by the time-dependent Dirichlet boundary condition

$$\phi = \begin{cases} 0 : & t \in [0, 1] \cup (1.1, 7.6] \cup (7.7, 14.2] \cup (14.3, 20.8] \text{ ms}, \vec{x} \in \Gamma_L \\ 3 : & t \in (1, 1.1] \cup (7.6, 7.7] \cup (14.2, 14.3] \text{ ms}, \vec{x} \in \Gamma_L \end{cases} \quad (6)$$

2.3.2 Transmembrane Flux Boundary Conditions

The transmembrane flux for the i^{th} ion specie (Equation 1) is incorporated into the model with a time, concentration, and voltage dependent Neumann boundary condition given by

$$F_i \cdot \vec{n} = f_i^{memb}(n_i, \phi, t), \vec{x} \in \Gamma_4, \quad (7)$$

where f_i^{memb} quantifies the transmembrane flux for the i^{th} ion, and is given by

$$f_i^{memb} = \frac{I_i}{z_i F}. \quad (8)$$

Note that this flux condition applies only to the Γ_4 boundary, which corresponds to the membrane wall within the node of Ranvier. This equation also incorporates a

Hodgkin-Huxley [64] based scheme to compute I_i , the transmembrane ionic current for the i^{th} ion specie. This model was adapted from Dione et. al. [43] to include calcium and chloride current [65,66]. These equations are unique due to an individual ion's Nernst potential and combinations of the gating variables, and are given by

$$I_{Na^+} = (g_{Na}^l m^3 h) \cdot (V - E_{Na}), \quad (9)$$

$$I_{K^+} = (g_K^l n^4) \cdot (V - E_K), \quad (10)$$

$$I_{Ca^{+2}} = (g_{Ca}^l m^2) \cdot (V - E_{Ca}), \quad (11)$$

$$I_{Cl^-} = (g_{Cl}^l) \cdot (V - E_{Cl}). \quad (12)$$

The transmembrane voltage, $V = \phi_I - \phi_E$, is computed along the node of Ranvier at each point in the discretized computational mesh (Figure 3). This voltage is then used to calculate the state of the gating variables m , n , and h via the Hodgkin-Huxley [64] system of ODEs given by

$$\frac{dn}{dt} = \alpha_n(V)(1 - n) - \beta_n(V)n, \quad (13)$$

$$\frac{dm}{dt} = \alpha_m(V)(1 - m) - \beta_m(V)m, \quad (14)$$

$$\frac{dh}{dt} = \alpha_h(V)(1 - h) - \beta_h(V)h. \quad (15)$$

The gating variables quantify probabilities that replicate the opening and closing of the neuron's voltage gated ion channels, and thus dictate ion channel permeability and subsequent transmembrane ionic flux.

Finally, the Nernst potential of the i^{th} ion, E_i , is given by

$$E_i = \frac{RT}{z_i F} \ln \left(\frac{n_i^{extra}}{n_i^{intra}} \right), \quad (16)$$

where g_i^l and g_i^v designate the conductance of the leak channels and voltage gated channels for each ion. Conductance values [43,44,65,66] used in the mathematical model are presented in Table 2.

Table 2: **Ion channel conductance parameters used in the calculation of membrane current.**

Parameter	Value
g_{Na}^v	1000.0 S/m ²
g_K^v	400.0 S/m ²
g_{Ca}^v	9.0 S/m ²
g_{Cl}^v	0.2 S/m ²
g_{Na}^l	0.175 S/m ²
g_K^l	0.50 S/m ²
g_{Ca}^l	0 S/m ²
g_{Cl}^l	0 S/m ²

2.3.3 Additional Boundary Conditions

The concentration of each ion is set to a constant bulk solution on the top boundary of the extracellular space, Γ_1 , [43,44] using the non-homogeneous boundary condition

$$n_i = n_i^0, \quad \vec{x} \in \Gamma_1. \quad (17)$$

For Equation 1, ion flux is set to zero on all boundaries other than the membrane using the homogenous Neumann boundary condition

$$F_i \cdot \vec{n} = 0, \quad \vec{x} \in \Gamma_2 \cup \Gamma_5 \cup \Gamma_L \cup \Gamma_R. \quad (18)$$

Finally, the charge density in Equation 3 is set to zero on the boundaries not governed by a TES or DBS source or ground:

$$\epsilon \nabla \phi \cdot \vec{n} = 0, \quad \vec{x} \in \Gamma_1 \cup \Gamma_2 \cup \Gamma_3. \quad (19)$$

2.4 Numerical Implementation

Equations 1 and 3 are decoupled using the Gauss-Seidel method [67]. The solution algorithm consists of the following steps:

1. Solve Equation 3 for ϕ at time step $k + 1$ given ion concentrations at time step k , n_i^k , with boundary conditions given by Equations 4, 5, and 19. Let ϕ^{k+1} denote this solution.
2. Solve for f_i^{memb} given n_i^k and ϕ^{k+1} (see Section 2.3.2).
3. Solve Equation 1 for n_i , for each ion type, at time step $k + 1$ given ϕ^{k+1} , with boundary

conditions given by Equations 17, 18, and 7. Let n_i^{k+1} denote these solutions.

The result is numerical solutions of ϕ and n_i at time step $k + 1$. This iterative sequence is initiated using prescribed intracellular and extracellular initial concentrations of each ion type, and is repeated until the end of the simulation. Within this loop, an inner iteration is used in step 2 to solve the Hodgkin-Huxley system with a smaller time step. This approach ensures the accuracy of the ion flux at the membrane and enables a larger time step for the more computationally intensive PDE solvers in steps 1 and 3. Given that the transmembrane voltage and subsequent flux vary along the node of Ranvier, a different realization of these ordinary differential equations (ODEs) is needed to be solved at every point along the membrane. In this work, the discretized domain generates 1,700 nodes along the membrane, thus the Hodgkin-Huxley ODE system was instantiated and solved 1,700 times at each simulation time step.

The PDE in step 1 is solved using the finite element method. The PDE system in step 3 is discretized in time using the θ -rule and space using the finite element method [68]. The value of θ was set equal to 1, which corresponds to the backward Euler method, due to its L-stability properties [69]. Resulting weak formulations for these equations are presented in Section 2.5. The Hodgkin-Huxley ODEs are solved using LSODE [69, 70]. This iterative implementation approach enables numerical solvers tailored to each individual equation to be used [71], as well as individualized time steps for the PDEs and ODEs.

2.5 PDE Weak Formulation Derivations

The derivations of the weak formulations for the Poisson and Nernst-Planck equations for the finite element method are shown here. A more in-depth description of the finite element method and other mathematical definitions are explained in Appendix A.

2.5.1 Poisson Equation

$$\text{Let } f = -F \sum_{i=1}^n z_i n_i$$

Given $f \in L^2(\Omega)$, multiply Equation 3 by an arbitrary test function, v , and integrate over the domain Ω :

$$\int_{\Omega} \nabla \cdot (\epsilon \nabla \phi) v \, d\Omega = \int_{\Omega} f(n) v \, d\Omega.$$

Applying Green's Theorem yields:

$$\int_{\Omega} \epsilon \nabla \phi \cdot \nabla v \, d\Omega = - \int_{\Omega} f(n)v \, d\Omega + \int_{\Gamma} v(\vec{n} \cdot \epsilon \nabla \phi) \, ds$$

Applying boundary conditions given by Equation 19 gives:

$$\int_{\Omega} \epsilon \nabla \phi \cdot \nabla v \, d\Omega = - \int_{\Omega} f(n)v \, d\Omega.$$

We stipulate the solution space to enforce the Dirichlet boundary conditions in Equations 4 and 5, and arrive at the weak formulation: Given $f \in L^2(\Omega)$, find $\phi \in H_0^1(\Omega)$ such that:

$$\int_{\Omega} \epsilon \nabla \phi \cdot \nabla v \, d\Omega = - \int_{\Omega} f(n)v \, d\Omega, \text{ for all } v \in H_0^1(\Omega),$$

where $H_0^1(\Omega) = \{u \mid u \in H^1(\Omega) \text{ and } u = 0 \text{ on } \Gamma_1\}$.

2.5.2 Nernst-Planck Equation

Discretize the time derivative in Equation 1 using the θ -rule:

$$\frac{\partial n_i}{\partial t} \approx \frac{n_i^{k+1} - n_i^k}{\Delta t} = \theta(-\nabla \cdot F_i^{k+1}) + (1 - \theta)(-\nabla \cdot F_i^k)$$

Given $F_i \in L^2(\Omega)$, multiply Equation 1 by an arbitrary test function v and integrate over Ω :

$$\int_{\Omega} n_i^{k+1} v \, d\Omega = \int_{\Omega} n_i^k v \, d\Omega - \theta dt \int_{\Omega} (\nabla \cdot F_i^{k+1}) v \, d\Omega - dt(1 - \theta) \int_{\Omega} (\nabla \cdot F_i^k) v \, d\Omega.$$

Applying Green's Theorem yields:

$$\begin{aligned} \int_{\Omega} n_i^{k+1} v \, d\Omega &= \int_{\Omega} n_i^k v \, d\Omega - \theta dt \int_{\Gamma} (F_i^{k+1} \cdot \vec{n}) v \, ds + \theta dt \int_{\Omega} F_i^{k+1} \cdot \nabla v \, d\Omega \\ &\quad - dt(1 - \theta) \int_{\Gamma} (F_i^k \cdot \vec{n}) v \, ds + dt(1 - \theta) \int_{\Omega} F_i^k \cdot \nabla v \, d\Omega. \end{aligned}$$

Applying boundary conditions given by Equations 18 and 7 gives:

$$\begin{aligned} \int_{\Omega} n_i^{k+1} v \, d\Omega - \theta dt \int_{\Omega} F_i^{k+1} \cdot \nabla v \, d\Omega &= \int_{\Omega} n_i^k v \, d\Omega - \theta dt \int_{\Gamma_4} f_i^{memb^{k+1}} v \, ds \\ &\quad - dt(1 - \theta) \int_{\Gamma_4} f_i^{memb^k} v \, ds + dt(1 - \theta) \int_{\Omega} F_i^k \cdot \nabla v \, d\Omega. \end{aligned}$$

We stipulate the solution space to enforce the Dirichlet boundary conditions in Equation 17 and arrive at the weak formulation: Given $F_i \in L^2(\Omega)$, find $n^{k+1} \in H_{n_i}^1(\Omega)$ such that:

$$\begin{aligned} \int_{\Omega} n_i^{k+1} v \, d\Omega - \theta dt \int_{\Omega} F_i^{k+1} \cdot \nabla v \, d\Omega &= \int_{\Omega} n_i^k v \, d\Omega - \theta dt \int_{\Gamma_4} f_i^{memb^{k+1}} v \, ds \\ &\quad - dt(1 - \theta) \int_{\Gamma_4} f_i^{memb^k} v \, ds + dt(1 - \theta) \int_{\Omega} F_i^k \cdot \nabla v \, d\Omega, \end{aligned}$$

for all $v \in H_{n_i}^1(\Omega)$.

2.6 Computational Tools

The computational domain (Figure 3) was constructed and discretized using GMSH [72]. The FEniCS computing platform [73] was used to solve the partial differential equations. This Python based library offers packages to solve finite element weak formulations subject to all boundary and initial conditions. In addition, Python’s SciPy library was used to access the LSODE method [74].

Given the complexity of the mathematical model and solution approach, an object-oriented implementation of the code was developed, as illustrated in Figure 4. This approach compartmentalizes major modeling components into ‘classes’, and in doing so, facilitates debugging as each class can be analyzed independently, and in addition, improves code readability. Furthermore, while object-oriented implementations often take more time to design and implement than traditional procedural implementations, a significant advantage of using a class-based structure is its inherent ability to support alternative applications. For example, changes in domain geometry, mesh resolution, neurostimulation treatment parameters, or even in the set of ions used can be effortlessly incorporated with virtually no changes to the software [75].

A class for the Nernst-Planck equation incorporates all information needed to solve this equation. This includes its associated weak formulation, diffusivity values, boundary conditions, time steps, and domain information. There are eight instantiations of this class, one for each ion type for both the intracellular and extracellular domains. A separate class is used to solve for f_i^{memb} needed in step 2 of the iterative solution algorithm. There is an instantiation of this class for each of the four ion types. These membrane current classes in turn possess an object dedicated to solving the Hodgkin-Huxley differential equations, which generates solutions for the gating variables m , n , and h (see Section 2.3.2). There are 1,700

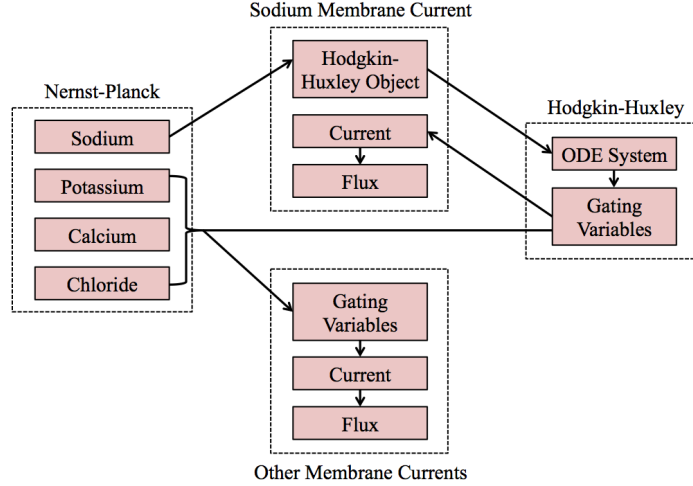


Figure 4: **Diagram illustrating the relationships between the different classes in the software.**

instantiations of this class, one for each discretized point on the membrane. Information in this Hodgkin-Huxley class is used by the membrane current class to resolve f_i^{memb} along the membrane, which is then used by the Nernst-Planck class via access to the membrane current class.

2.7 Numerical Simulations

For the comparison between TES and DBS, the same initial conditions, domain, simulation time, and numerical implementation are used for both simulations. This implementation allows for direct comparison of the two treatments. A time step of 0.01 ms was selected for the outer iteration of the solution algorithm (2.4) as this value is small enough to accurately model the changes in electric potential and ion concentrations [44]. For solving the inner iteration of step 2, the ODE system was solved with a maximal time step of 0.0005 ms.

A major difference between these two therapies is the nature of electric current that is applied. The simulations incorporate the different nature of these electric currents through the use of a different boundary condition on the left side of the extracellular space for the Poisson equation (Equation 3) as described by Equation 5 for TES and Equation 6 for DBS.

First, a simulation of TES was performed via the boundary condition given by Equation 5. As described by Equation 5, TES is simulated by changing the Dirichlet boundary condition value from 0 V to 0.1 V on the left boundary of the extracellular space after $t = 1$ ms; this dosage is consistent with electric potentials achieved during TES sessions [61–63]. This allows the electric potential, transmembrane voltage, ion channel gating variables, ionic flux, and ion

concentrations before and after electrical stimulation to be directly compared, thus enabling a direct assessment of the specific impact of TES on neuronal electrodynamics. Then, for the DBS simulation Equation 6 is enforced on the left boundary of the extracellular space.

All parameter values used in the model and simulations (see Tables 1 and 3) are taken from published biomedical literature and previous neuronal-based mathematical models [43, 44, 56].

Table 3: **Neurostimulation treatment (stimulus amplitude, frequency, and duration) and simulation (time step, simulation length) parameters**

Parameter	Value
Time Step	0.01 ms
Hodgkin-Huxley Time Step	0.0005 ms
Simulation Start	0 ms
Start Time of DBS and TES Application	1 ms
Total Simulation Time	20.8 ms
TES Stimulus Amplitude	0.1 V
TES Stimulus Duration	19.8 ms
DBS Stimulus Amplitude	3 V
DBS Stimulus Duration (Pulse Width)	0.1 ms
DBS Stimulus Frequency	150 Hz

An iterative implementation and testing approach was used to verify the accuracy of the model implementation. First, individual solvers for the PDEs given by Equation 1 and Equation 3 were constructed and validated against the online PDE solver DiffpackSE [76, 77]. Second, the Hodgkin-Huxley ODE model was implemented and verified independently of the PDEs, thus ensuring that changes in intracellular and extracellular electric potential and ion concentrations at the membrane correctly compute gating variable states as well as flux during membrane polarization [64–66]. Third, these three solvers were integrated into a single solution code using the object-oriented approach as detailed in Section 2.6. Fourth, verification of the complete code came by comparing sodium and potassium membrane flux time courses and magnitudes to results from previous PNP modeling implementations [43, 44, 56]. Fifth, the transmembrane voltages, intra/extra-cellular ion concentrations, ion channel gating variables, and membrane current fluxes predicted by the complete, fully-coupled model were compared to the isolated Hodgkin-Huxley code to validate the accuracy of the fully integrated, coupled implementation used in all simulations. Finally, we draw comparisons between our results and those of published medical studies and biological experiments when available.

3 Transcranial Electrical Stimulation Results

3.1 Transmembrane Voltage Polarization Exhibits Location Specificity

The electric potential energy, ϕ , throughout the neuronal domain at both the beginning and the end of the simulation is shown in Figure 5. Here, changes in both the distribution and magnitude of ϕ from TES are observed. In particular, prior to neurostimulation application, the electric potential distribution is highly symmetric (Figure 5A), however, after TES administration, the domain is highly asymmetric; the majority of high voltage areas are concentrated on the left side of the domain, juxtaposed with the stimulation source boundary condition $\phi = 0.1$ V, and electric potential declines more rapidly as the ground boundary is approached (Figure 5B). In addition, the maximum extracellular electric potential value increases by 55.2% from 0.096 V at the start of the simulation to 0.149 V at the end, which due to ionic electrodiffusion, is 49.0% greater than the anode source voltage of 0.1 V. Further, intracellular values for ϕ increase themselves from a minimum and maximum of 0.020 V and 0.026 V to 0.063 V and 0.078 V, respectively.

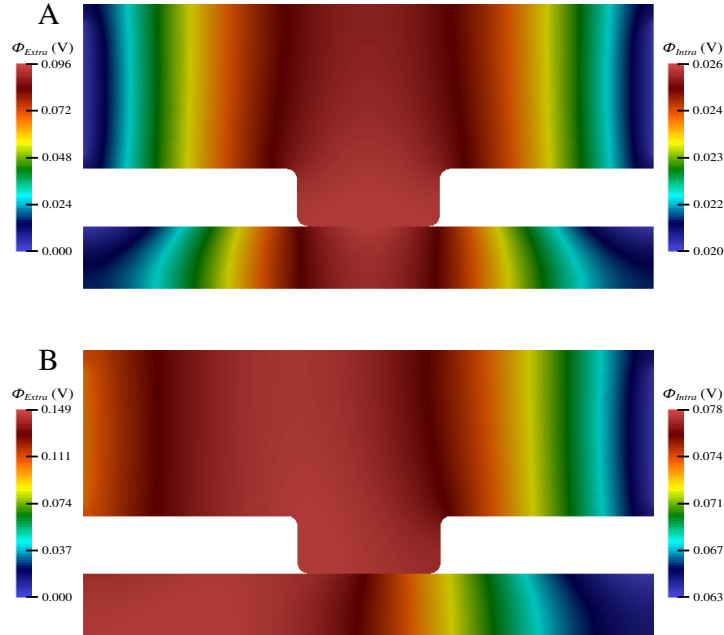


Figure 5: **Electric potential energy (ϕ) throughout the computational domain during TES treatment.** The distribution of electric potential is shown at $t = 0$ ms (A) and $t = 20$ ms (B). Illustrates the Dirichlet boundary conditions used to simulate TES treatment with a ground of $\phi = 0$ on left and right extracellular boundaries prior to treatment and then a left boundary of $\phi = 0.1$ during treatment to simulate the stimulation source on the left side of the domain.

Along the neuron membrane, there is a change in transmembrane voltage upon

application of electrical stimulation after $t = 1$ ms (Figure 6). Figure 6A shows the transmembrane voltage throughout the simulation at 11 equispaced points within the node of Ranvier. These points are labeled as a percent based on their position along the node of Ranvier where, for example, 0%, 50%, and 100% refer to the points on the far left, middle, and far right of the node. The resting transmembrane voltage for each of these points is approximately -70.23 mV. For the point in the center of the node the transmembrane voltage does not change upon stimulation, maintaining its value of -70.23 mV throughout the simulation. For all other points, immediately at stimulation application, there is an instantaneous jump in transmembrane voltage. However, this change depends on the location along the membrane (Figure 6B).

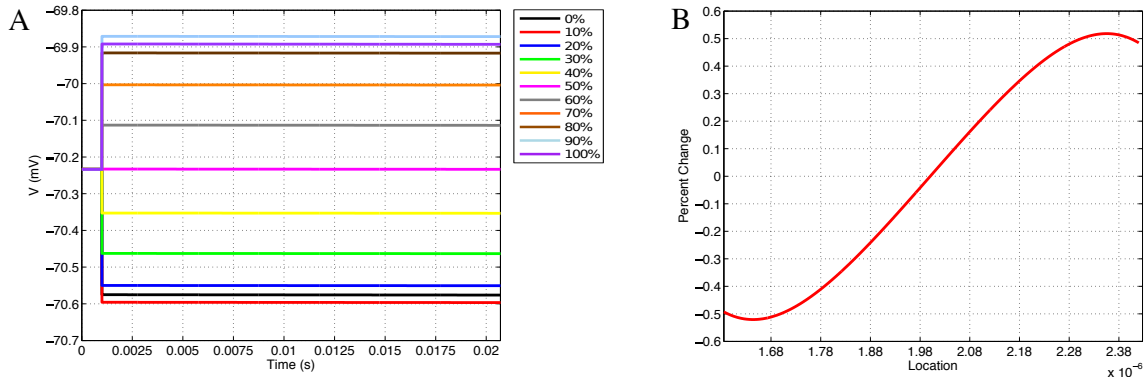


Figure 6: **Transmembrane voltage during TES treatment.**

(A) Transmembrane voltages due to TES application at equispaced locations within the node of Ranvier. Positions labeled with 0%, 50%, and 100% being the far left, middle, and far right of the node, respectively. (B) Percent change in the transmembrane voltage due to TES at each point along the membrane. A positive percent change indicates depolarization and a negative percent change indicates hyperpolarization.

These results demonstrate the location dependence of changes in transmembrane voltage due to TES. Specifically, transmembrane voltages at points left of center become hyperpolarized, whereas depolarization occurs on the right-hand side. In addition, the magnitude of the polarization from TES administration varies depending on proximity to the edges and center of the node of Ranvier; these values change to a greater degree near the edges as compared to locations near the center. Furthermore, maximum changes in transmembrane voltage do not occur at the extreme edges of the node, but rather at locations situated at $1.64 \cdot 10^{-6} \mu\text{m}$ and $2.35 \cdot 10^{-6} \mu\text{m}$, which correspond to approximately 9% and 91%, both well within the the edge of the node of Ranvier. Interestingly, hyperpolarization occurs for locations on the side with the 0.1 V stimulation source, whereas depolarization occurs on

the side adjacent to the ground boundary condition.

In addition to these findings, it is observed that membrane voltage polarization is sustained throughout the TES application, which is consistent with clinical results that TES effects persist in sessions consisting of tens of minutes [32, 78]. This sustained increase in neural impulse sensitivity in specific regions of a node of Ranvier permits the TES treatment efficacy recognized by the medical field [7, 32]. Our results are also consistent with clinical research that shows that TES has the net effect of increasing neuron excitability by depolarizing to sub-threshold potential [25–28]. In addition, changes in transmembrane voltage magnitude are consistent with previous mathematical simulations of TES [42].

3.2 Voltage Gated Ion Channel State Variables Exhibit Location Specificity

The changes in transmembrane voltage due to TES directly impact the behavior of voltage gated ion channels due to changes in their gating variables (Figure 7). Like Figure 6A, Figure 7 displays the values of each gating variable throughout the simulation at the same 11 equispaced points within the node of Ranvier. The location specificity previously observed with transmembrane voltage is also present for the changes in all gating variables.

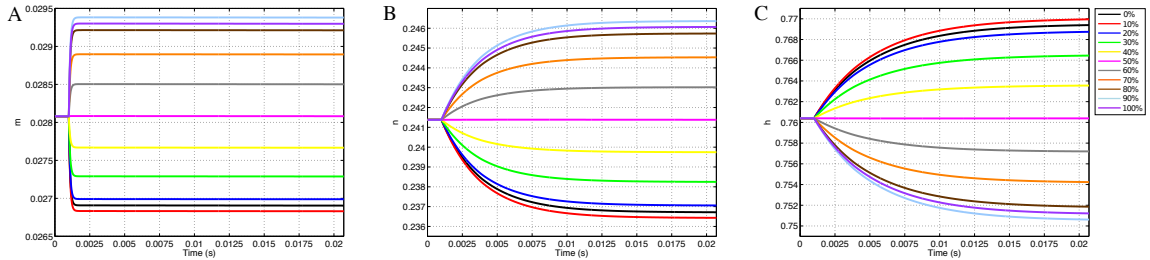


Figure 7: **Gating variable values due to TES application at equispaced locations within the node of Ranvier.**

Prior to stimulation, m , n , and h show minimal position dependence as their respective values are essentially equal throughout the membrane. For example, before TES application, m is approximately 0.0281 everywhere in the node of Ranvier. When stimulation is applied, changes in m , n , and h become location specific, points where the cell becomes hyperpolarized, i.e. locations between 0% and 50%, result in decreases in m and n as well as increases in h . On the other hand, at sites of depolarization, namely positions between 50% and 100%, m and n increase while h decreases.

Corresponding to the locations of maximum change in transmembrane voltage, positions of greatest change in all gating variables also occur off of the membrane edges near 10% and

90%. In addition, the curves of the gating variables are directly associated to the polarized membrane voltages at the same 11 points. In particular, the amplitudes of the gating variable curves correspond to their associated transmembrane voltages, as well as distances between the curves. More precisely, the ranking of each curve of m based on plot amplitude is identical to the ranking of the transmembrane voltage curves. In addition, the amount of spacing between m curves (Figure 7A) is proportional to the spacing between transmembrane voltage curves (Figure 6A). The same observations apply for n (Figure 7B), and h (Figure 7C) as well with the exception that the ordering is inverted due to characteristics of h .

While dependence of gating variables on transmembrane voltage is not unexpected, location specificity of the gating variables due to TES is novel, and begins to explain how neurostimulation impacts ion channel gating and subsequent ionic flux. Of particular interest in this regard, a clear difference in the shapes, magnitudes and trajectories of the m , n , and h time course curves is observable; the m gating variable changes rapidly, hitting a limiting value early in the simulation, whereas n and h grow more slowly, and fail to reach an asymptotic value within 20 ms. However, m has the lowest amplitude change of the three, with a maximum change of 0.0013, which is only 26.1% and 16.25% of the changes in n and h , respectively.

Figure 8 shows the values of each gating variable at every point along the discretized membrane at seven different simulation times. At $t = 2$ ms, each gating variable maintains the same value along the membrane as TES application has not yet started; after administration, the value of each gating variable changes over time based upon its location in the membrane. The speed at which m reaches its limiting value is also seen here as the curves for 5 ms, 10 ms, and 20 ms are virtually identical. In contrast, all curves for n and h are visible and continually change throughout the 20 ms simulation. Similar to transmembrane voltage, maximum and minimum values occur approximately at the 9% and 91% locations. Furthermore, it is seen that on the left-half of the node of Ranvier, the m and n probability values are lower than those attained on the right-half, and the opposite is true for h . As will be shown in Section 3.3, the time and location dependence of changes in these gating variables as a result of TES has a direct impact on transmembrane ionic current.

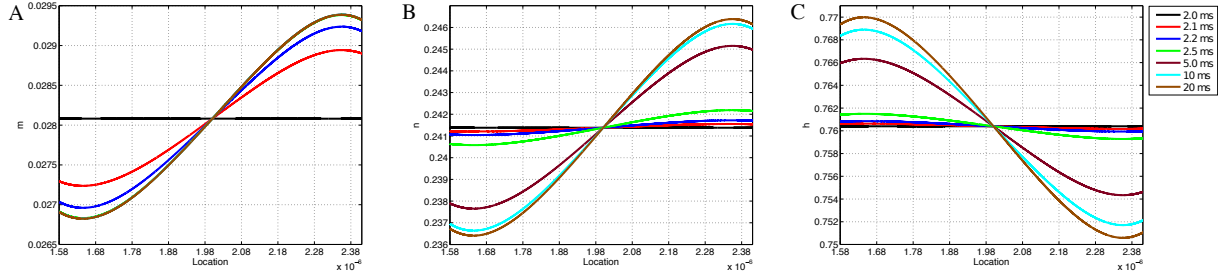


Figure 8: **Gating variable values during TES at each location along the node of Ranvier at simulation times $t = 2.0, 2.1, 2.2, 2.5, 5, 10,$ and 20 ms. (A) shows m , (B) shows n , and (C) shows h .**

3.3 Membrane Ion Flux Exhibits Location Specificity

As the gating variables dictate ion channel permeability, the location specificity observed in transmembrane voltage as well as m , n , and h has a direct influence on ion flux into and out of the neuron. Figure 9 shows the ion flux for sodium, potassium, and calcium over time at the 11 equispaced points within the node of Ranvier. Given the sign convention of the boundary condition governing membrane current (Equation 7), a negative value for flux indicates current coming into the cell from the extracellular space.

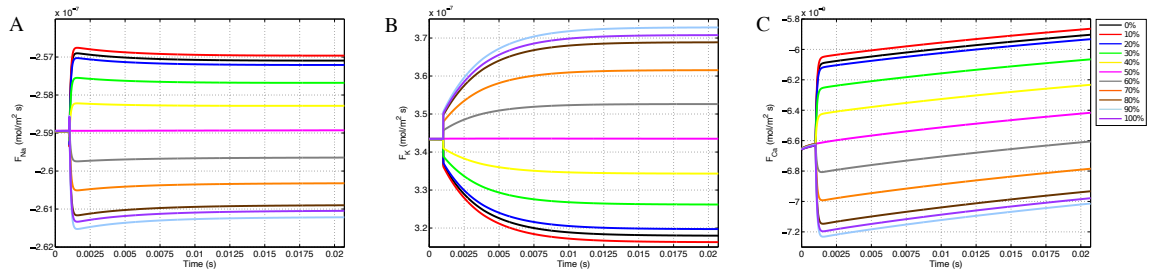


Figure 9: **Transmembrane ionic flux due to the application of a TES stimulus.** Membrane flux for sodium (A), potassium (B), and calcium (C) over the course of the simulations for the 11 equispaced points on the node of Ranvier. A negative flux indicates ion flow into the cell from the extracellular space, and a positive value indicates an efflux out of the cell.

Due to passive electrodiffusion forces from the multi-ion environment, as well as a transmembrane voltage not precisely equal to -70 mV, a slight flux of ions across the membrane occurs prior to TES application. Upon activation after $t = 1.0$ ms, there are significant changes in neuronal flux. For locations on the right-half of the node of Ranvier, where the cell becomes depolarized (Figure 6B), there is an increase in sodium influx (Figure 9A). This is precisely predicted by the gating variable results (Figures 7A and 7C); as m represents sodium channel activation, which increases on the right-hand side, and h , sodium channel inactivation, which decreases on the right, an increase in sodium influx is this region

is expected, and as shown in Figure 9A is attained. In addition, this influx is greatest at the 91% mark, which correlates with all prior results including (i) where the cell experiences its greatest depolarization, (ii) where m is maximal, and (iii) where h is minimal. On the hyperpolarized left-hand side, sodium influx still occurs, but at a decreased rate as m decreases and h increases here.

The m gating variable also controls calcium channel activation (see Section 2.3.2), and so trends in calcium flux function similarly to sodium flux (Figure 9C). Specifically, locations where the cell becomes depolarized yield an increase in calcium influx and hyperpolarized regions experience a decreased influx. For potassium, due to its reversal potential, the opposite occurs and an efflux transpires throughout the entire node of Ranvier. In addition, as n governs potassium activation, potassium efflux increases on the left side where hyperpolarization presents and decreases on the right half of the node of Ranvier (Figure 9B).

These results are consistent with published TES studies that show an increase in calcium influx from a membrane depolarization due to an electric field applied in the extracellular medium [29,31]. In addition, like the biological literature, our model predicts that this influx is governed by voltage gated calcium channel permeability [30]. The novelty of this model is in extending this knowledge to provide a description of how the voltage gated calcium channels within the node of Ranvier operate to achieve this. First, the model allows to see the changes in flux at a greater frequency and with more spacial detail than has been captured with experiments. In addition, the model identifies the gating variable m as driving the changes in flux. Finally, these results reveal a time and spatial based dependence of the gating variable, voltage gated channel activation, and calcium flux.

3.4 TES Causes Intracellular Calcium Dyshomeostasis

As shown in Section 3.3, calcium flows into the neuron from the extracellular space at different rates depending on the region within the node of Ranvier (Figure 9C). Thus, over the course of the TES simulation, an increase in intracellular calcium concentration occurs. However, the magnitude and rate of this increase is unknown. Figure 10 shows intracellular calcium concentrations at six simulation time steps. At $t = 0$ ms, the entire intracellular space has a constant concentration of 10^{-4} mM, which is the initial condition for calcium in this domain. Over time, an increase in calcium concentrations from calcium flux due to TES is seen at all subsequent time steps. In addition, for times $t > 0$, a larger concentration of calcium is

noticed at the membrane region, precisely due to calcium influx at the membrane, along with a diffusion throughout the intracellular domain. At the 91% membrane location calcium concentrations increase by 71.65% over the course of the simulation. Furthermore, the total amount of calcium within the intracellular space increases by 63.86% during the course of the simulation. This increase is approximately linear, as can be seen from the color gradients of the intracellular concentration plots.

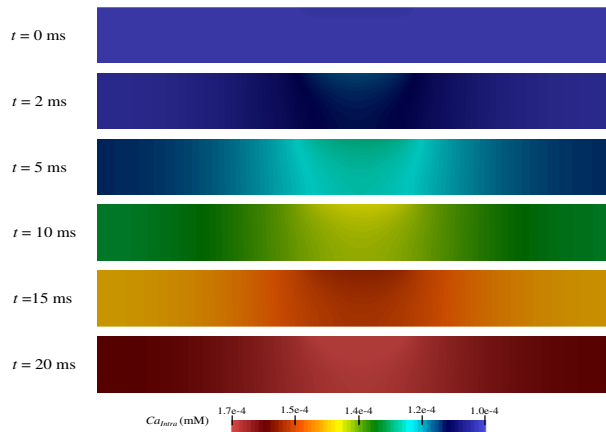


Figure 10: Concentration of calcium in the intracellular space (Ω_I in Figure 2) during the simulation at times $t = 0, 2, 5, 10, 15,$ and 20 ms. Visualizes the increase in intracellular calcium concentrations as a result of the TES-induced calcium influx.

These results are consistent with prior experiments that found an increase in calcium concentration due to an influx of calcium in the presence of electrical stimulation [30,31]. In fact, the values predicted by the model are within one order of magnitude of those shown in electrical stimulation biological studies [31]. Moreover, the model augments this knowledge by providing a detailed prediction of how, where, and when calcium ion flow into the neuron as described in Section 3.3.

4 Deep Brain Stimulation and Comparison Results

4.1 Instantaneous Transmembrane Polarization

The electric potential energy (ϕ) throughout the intra- and extracellular regions of the domain is shown in Figure 11. The electric potential before the neurostimulation treatment begins at 1 ms is identical for both simulations (TES and DBS) and is shown in Figure 11A. When the treatments begin at a time of 1 ms there are immediate changes in the electric potential distributions for both DBS (Figure 11B) and TES (Figure 11C) due to the different value for

the Dirichlet boundary used to model the amplitude of the electrode. The value of this Dirichlet boundary is clear from these figures, for DBS this value is 3 V (Equation 5) and for TES it is 0.1 V (Equation 6), as observed in the color of the left side of the extracellular space in Figures 11B and 11C respectively. Clearly, there are notable differences in the electric potential magnitude and distribution with and without the neurostimulation as well as between these two modes of neurostimulation.

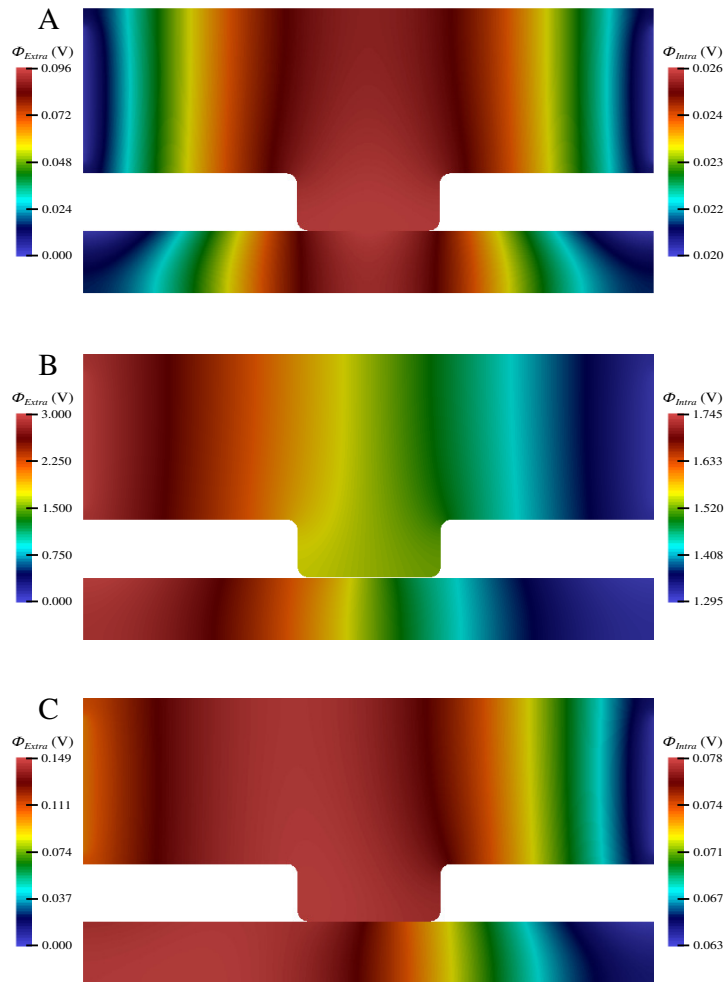


Figure 11: **Comparison of electric potential energy throughout the domain.** A: Electric potential at the beginning of the simulations (same for both TES and DBS). B: Electric potential energy throughout the domain for DBS during the first pulse application time = 1.1 ms. C: Electric potential energy throughout the domain for TES after the current is applied, time = 1.1 ms.

One major difference in these electric potential figures is the location within the domain where the highest voltage areas are concentrated. Prior to the neurostimulation application (Figure 11A), the highest voltage is concentrated in the center of the domain as the lowest voltage ($\phi = 0$ V) regions are the far left and right edges of the extracellular space. With DBS (Figure 11B) the highest voltage area is concentrated on the left side of the domain,

juxtaposed with the stimulation source boundary condition $\phi = 3$ V. With TES (Figure 11C) the electric potential distribution is highly asymmetric with high voltage areas that are larger and concentrated just left of the center of the domain. Also, the color distribution appears more symmetric and evenly distributed with DBS whereas in the TES figure the electric potential changes more rapidly on the side approaching the ground boundary.

The application of a DBS current causes an instantaneous polarization of the cell's membrane potential, as shown in Figure 12. Figure 12A shows the transmembrane voltage throughout the simulation at 11 equispaced points along the node of Ranvier. Each location is labeled in terms of its percent into the node with 0%, 50%, and 100% being the far left, middle, and far right respectively. The neuron begins at with a resting membrane potential of -70.23 mV, but when the stimulus is turned on at a time of 1 ms this transmembrane voltage experiences an immediate polarization, where the value either increases or decreases for the duration of the current pulse. When the current pulse is turned off at 1.1 ms the transmembrane voltage immediately returns to its initial value. This instantaneous polarization coincides with when the DBS current is applied occurs for each of the three pulses.

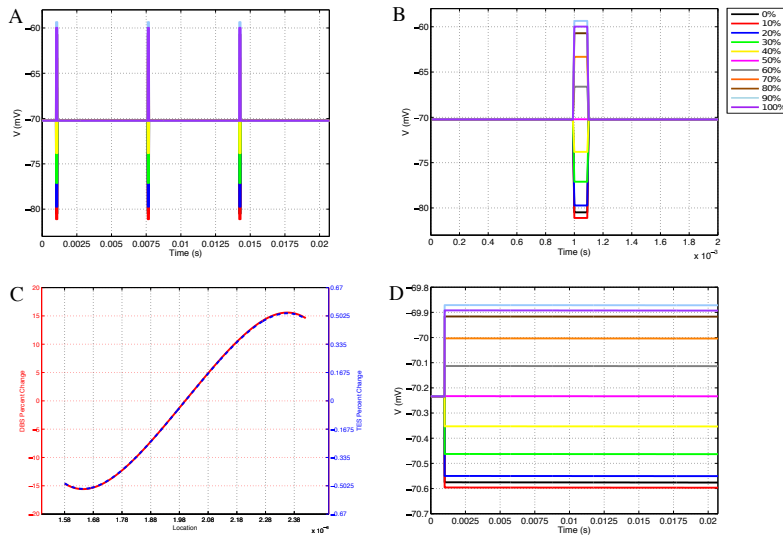


Figure 12: **Transmembrane voltage during DBS and TES treatment.** A: Transmembrane voltage throughout DBS simulation at 11 equispaced locations within the node of Ranvier. B: Transmembrane voltage during the first DBS pulse to better illustrate the distribution of the position curves during each pulse. C: Percent change in transmembrane voltage between when the current is off versus on at each point along the membrane for DBS (red, left axis scale) and TES (blue dashed line, right axis scale). $1.585 \cdot 10^{-6}$ μm is the far-left, $2 \cdot 10^{-6}$ μm is the center, and $2.385 \cdot 10^{-6}$ μm is the far right. A positive percent change indicates depolarization and a negative percent change indicates hyperpolarization. D: Transmembrane voltage throughout TES simulation at the same 11 locations.

As with TES, DBS exhibits location specificity in the changes in transmembrane

voltage, that is, the type and magnitude of this polarization depends on the location along the node of Ranvier. During each application, positions on the left side of the membrane become hyperpolarized while locations on the right half of the node become depolarized. As shown in Figures 12B and D the distribution of the curves during the electric current application look almost identical between DBS (Figure 12B) and TES (Figure 12D) other than, of course, the magnitude of the changes. The spacing between each curve is proportionate as well as the order of each curve is the same between DBS and TES, indicating that the locations that experience the largest hyperpolarization and depolarization are the same in each of these two treatments. Specifically, out of these 11 positions the largest changes in transmembrane voltage for both TES and DBS occur at 10% and 90%, not at the extreme 0% and 100%. In addition, the distribution of the potential curves for both TES and DBS are symmetric with the curves from 0% to 50% being a near perfect reflection of the curves from 50% to 100%.

Figure 12C shows the percent change in transmembrane voltage for both TES and DBS at each point along the node of Ranvier. For DBS the percent change is calculated based on the transmembrane voltage during the first pulse whereas TES uses the value at the end of the simulation since the change in transmembrane voltage is maintained throughout. This plot uses a different axis scales for each TES and DBS given the major difference in the degree of change for each treatment. As observed in the figure, the curves line up perfectly, meaning that the points with the minimum, maximum, and no change in transmembrane voltage occur in the exact same locations for both forms of neurostimulation. These curves are identical other than the magnitude of the changes, showing the major similarities in how DBS and TES polarize the transmembrane voltage at each point along the node.

Given that TES applies only a low dose of current while DBS administers a more direct, higher dose it is reasonable that the changes in transmembrane voltage are much larger in DBS than TES. Specifically, in the TES simulation the maximum percent change in transmembrane voltage is 0.52% while in DBS it is 15.58%. Thus, the transmembrane voltage during TES gets only as low as -70.60 mV and as high as -69.87 mV while with DBS transmembrane voltage experiences a range from -81.10 mV to -59.34 mV. This maximal value of transmembrane voltage of -59.36 mV is near the threshold of -55 mV required to fire an action potential. Thus, DBS raises the membrane potential in some location close to the threshold, supporting the treatment's ability to increase the possibility of action potential generation.

Another major difference between the treatments is the duration of the polarization. For

TES, polarization is sustained for the whole simulation due to the fact that the current is applied throughout the treatment session. On the other hand, DBS polarization occurs in pulses where the polarization turns on and off with the DBS stimulus. Thus, while the DBS-induced changes in transmembrane voltage are much greater, they only last for 0.1 ms, after which they return to their initial value, whereas TES-induced polarization persists for the whole simulation.

4.2 Asymmetric Location Specificity in Ion Channel Gating Variables

Figure 13 shows the values of the gating variables m , n , and h throughout DBS treatment at the same 11 equispaced points along the node of Ranvier as shown in Figure 12. These gating variables are probabilities between 0 and 1 that indicate ion channel state, controlling the opening and closing of the voltage gated channels.

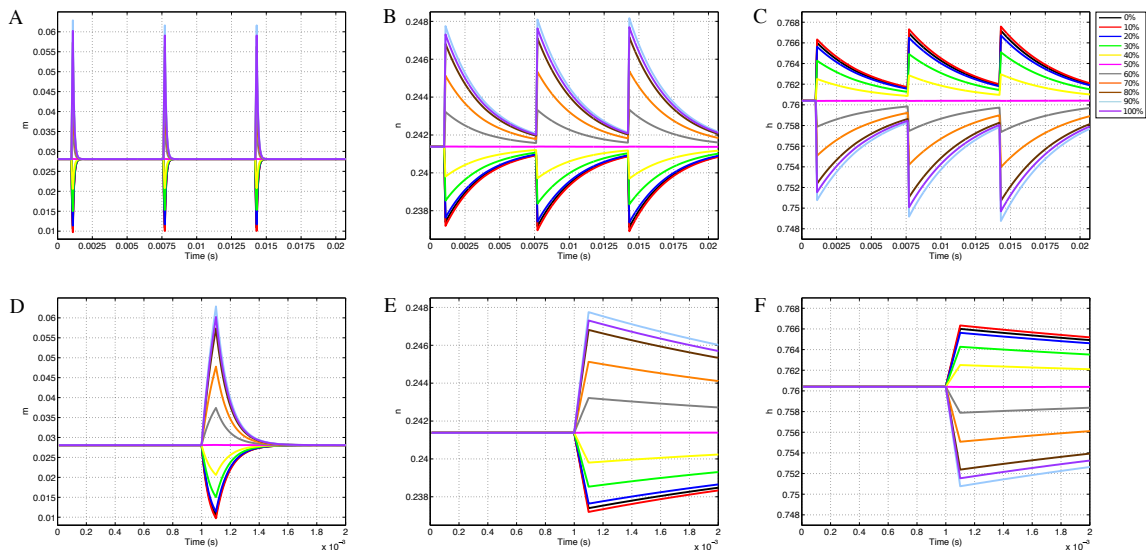


Figure 13: **Gating variables at equispaced positions along the node of Ranvier during DBS treatment.** A-C: Gating variables m (A), n (B), and h (C) throughout the whole simulation. D-F: Gating variables m (D), n (E), and h (F) during the first 2 ms of the simulation, showing their behavior during the first of three DBS pulses.

The location specificity observed in the transmembrane voltage results contribute to similar position-dependent effects on voltage gated ion channel states, m , n , and h . As a result of DBS, these gating parameters exhibit either increases or decreases depending on the location along the node of Ranvier. Each increase/decrease corresponds to the direction of the change (hyper/de-polarization) in transmembrane voltage as well as the magnitude, which was also observed in TES. Locations where the membrane potential becomes depolarized exhibit

increases in m and n along with decreases in h . On the other hand, hyperpolarized locations display the opposite behavior, with m and n decreasing in value while h increases. The order of curves for m and n are the same as that of V , meaning that the positions that exhibit the largest increases, no change, and largest decreases in m and n correspond to the same locations that display the largest increases, no change, and largest decreases in transmembrane voltage as well. This relationship is similar, but reversed for h . For example, the 10% location is the most hyperpolarized and this location also exhibits the smallest value of m and n along with the largest value of h .

TES showed similar location dependence, but with TES the increases and decreases in the gating variables were mostly symmetric whereas in DBS there is more asymmetry. Interestingly, the changes in transmembrane voltage (Figure 12) are highly symmetric for DBS (as well as TES), but yet for DBS the subsequent changes in the gating variables are asymmetric even though the gating variables in the TES simulations maintained the symmetric patterns. This difference can be observed in Figure 14, which compares the changes in the gating variables between TES and DBS at the same locations on the membrane. For example, as seen in Figure 14A, with TES the magnitude of the increase in h at the 10% position is approximately equal to the decrease in h at the 90% position. However, when looking at the same positions for DBS it is clear that the decrease in h at 90% exceeds the corresponding increase at 10%. Similarly, with m and n (14D and G) the TES curves at 90% and 10% exhibit roughly equal increases and decreases, but with DBS the increases in m and n at 90% are greater than their decreases at 10% (the corresponding point on the opposite side of the membrane).

This same symmetry for TES and asymmetry for DBS is also observed for other location pairs such as 25% and 75% as well as 40% and 60% in Figure 14. The asymmetry in the changes in gating variables in DBS can also be observed in Figure 13. In these figures it is clear that the increases in m and n on the right hand side of the membrane (50% to 100%) exceed the decreases on the left (0% to 50%) meanwhile the increases in h are less than the corresponding decreases.

Table 4 also demonstrates this asymmetry in the gating variable changes for DBS, specifically at the 10% and 90% locations. With TES, the change in the gating variables at these locations are equal, such as m increasing by 0.001 at 90% and decreasing by the same amount at 10%. On the other hand, with DBS these values are not the same. For example, m

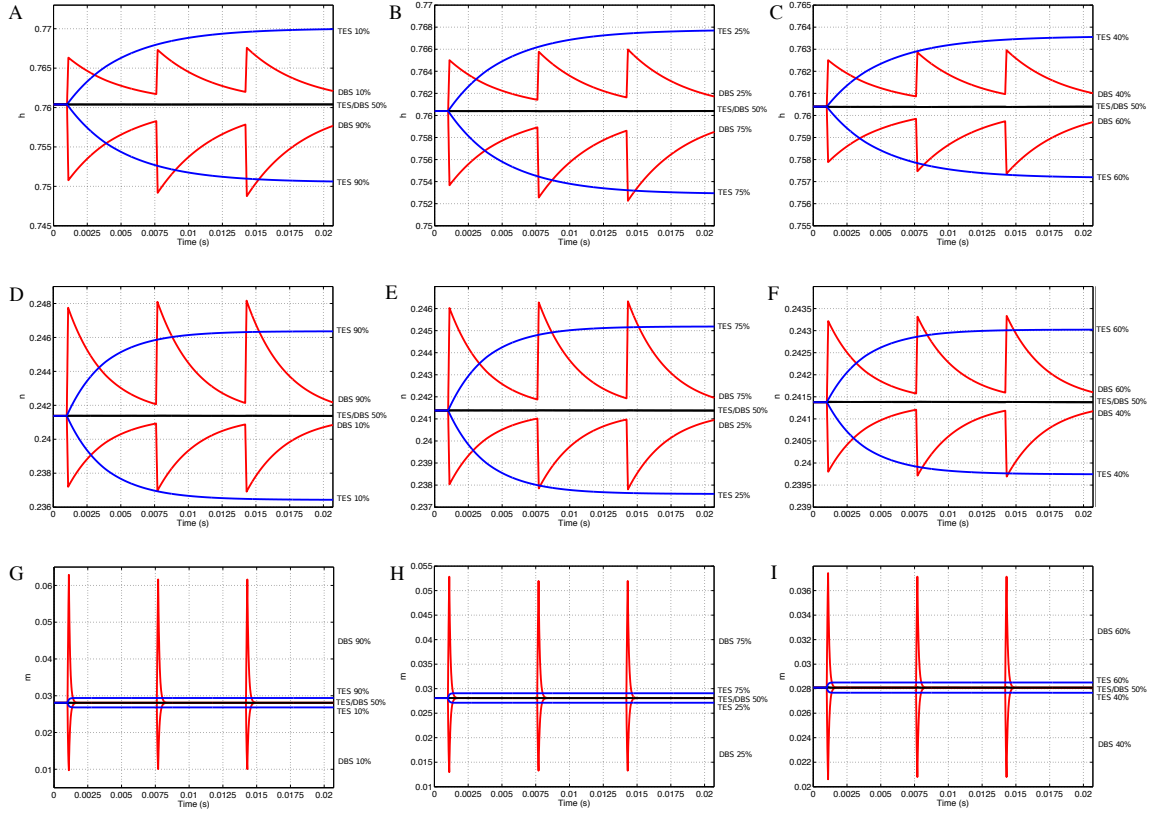


Figure 14: **Comparison of changes in gating variables between DBS and TES.** Plots comparing the behavior of the gating variables h (A-C), n (D-F), and m (G-I) overtime during DBS (red curves) and TES (blue curves) treatment. A, D, and G show the gating variables for each treatment at the 10% and 90% locations while B, E, and H show the 25% and 75% positions and finally C, F, and I display the gating variables at 40% and 60%. Each plot also includes the 50% location for TES and DBS (shown in black) to provide a reference of the location that exhibits no change.

increases by 0.035 at 90%, but only decreases by 0.018 (just over half as much) at 10%.

Table 4: **Asymmetry in changes in DBS gating variables.**

	DBS		TES	
	90%	10%	90%	10%
m	0.035	-0.018	0.001	-0.001
n	0.006	-0.004	0.005	-0.005
h	-0.010	0.006	-0.010	0.010

Table notes: This table shows the change in each gating variable at the 90% and 10% membrane locations from the start of the simulation to the maximum value it achieves during stimulation for both TES and DBS. A positive value indicates an increase in the value of the gating variable whereas a negative value signifies a decrease.

4.3 Speed of Changes in Gating Variables

As with the instantaneous change in transmembrane voltage observed in Figure 12A the gating variables also begin to change precisely when each stimulus is applied. But unlike transmembrane voltage that exhibits a sharp jump, the gating variables increase/decrease more gradually. Similarly, when the current pulse is turned off the gating variables do not immediately jump back to their initial value like transmembrane voltage does, instead they recover more slowly. Interestingly, the gating variables each have a distinct recovery speed. Particularly, m recovers much faster than both n and h , which both are much slower in returning back towards their initial value. The gating variable m increases up to 0.05 during the first stimulus pulse and then at a time of 2 ms, 0.9 ms after the first stimulus is turned off, m has already returned to its initial value of 0.028. On the other hand, n and h never fully recover to their initial value during the 6.5 ms between the DBS pulses. Thus, when the second pulse begins at 7.6 ms n and h are at slightly different values than they were at the start the simulation.

The different speeds of these changes between the different gating variables is also observed in the TES simulations where in a 20 ms simulation m reached its limiting value only 1 ms after the stimulus application while n and h continued to change throughout the remaining 19 ms of the simulation. Thus, it is clear that m changes more quickly than the other two gating variables, both when changing to a new value upon external current application and when returning to its resting value when the stimulus is turned off.

Another impact of the differing speeds at which the gating variables change is the observed in the comparison of the magnitude of changes in m , n , and h between TES and DBS. Figure 14 shows the changes in each gating variable at the same points (10%/90%, 25%/75%, and 40%/60%) in both TES and DBS to compare the magnitude of the changes between the two treatments. Clearly, m experiences greater changes in DBS than TES, for example 0.034 more at the 90% location. On the other hand, n and h change about the same in DBS as they do in TES.

This difference is somewhat surprising because the magnitude of changes in transmembrane voltage are significantly greater in DBS than TES. However, the DBS current is only applied for 0.1 ms at a time, which does not leave the slower-changing n and h much time to adjust. Presumably, if a DBS-amplitude pulse were applied for a longer period of time, then n and h would increase/decrease significantly more than they do in TES and in the

short (0.1 ms) pulse modeled here. As explained earlier, m changes faster than both n and h so even in the short DBS pulse of 0.1 ms m achieves a higher value than in does in the longer TES stimulation.

Another difference between the gating variables is which of the three pulses in which they reach their maximum value. For m the most change occurs in the first pulse, reaching a value of 0.063. In the other two pulses, m changes slightly less (as observed in the slightly lower second and third peaks in Figure 13A) reaching a value of 0.061, even though the amplitude of the electric current pulse is the same and the transmembrane voltages change by the same amount. On the other hand, n and h reach their maximum values (most extreme peaks) in the final pulse, as observed in the fact that each subsequent peak is higher than the last. One plausible explanation for this difference is the fact that n and h do not fully return to their initial value by the time the next pulse begins so their value is already starting closer to their last peak so when they change with the next pulse they achieve a higher value than the previous peak.

4.4 Transmembrane Ionic Flux

The DBS and TES-induced changes in transmembrane voltage and ion channel state influence the transmembrane flux for each ion. These changes in transmembrane flux for sodium, calcium, and potassium at the 11 equispaced points along the node of Ranvier throughout the simulation for both DBS and TES are shown in Figure 15. The pulse-like behavior of transmembrane voltage and the gating variables (especially m) generate similar bursts of responses in transmembrane flux. As a result of the DBS-induced electric current, each time the stimulus is applied there are major increases and decreases in flux. When the stimulus is removed the fluxes begin to return to their initial value (Figures 15A-C and D-F). The curves for each ion's flux exhibit different patterns of behavior, which can be explained by each ion's unique equation for flux (Equations 9-12) with distinct combinations of the gating variables and different Nernst potentials.

One major difference between the ions is the shape of the flux curves for the 0.1 ms that the pulse is applied. During the DBS pulse (1 to 1.1 ms), Ca^{+2} flux (Figures 15B and E) exhibits smooth changes, with an almost parabolic shape for points on the left side of the node (where calcium influx decreases). Meanwhile, calcium flux changes in a seemingly linear fashion for points on the right side of the domain (50% to 100%) where there is a substantial

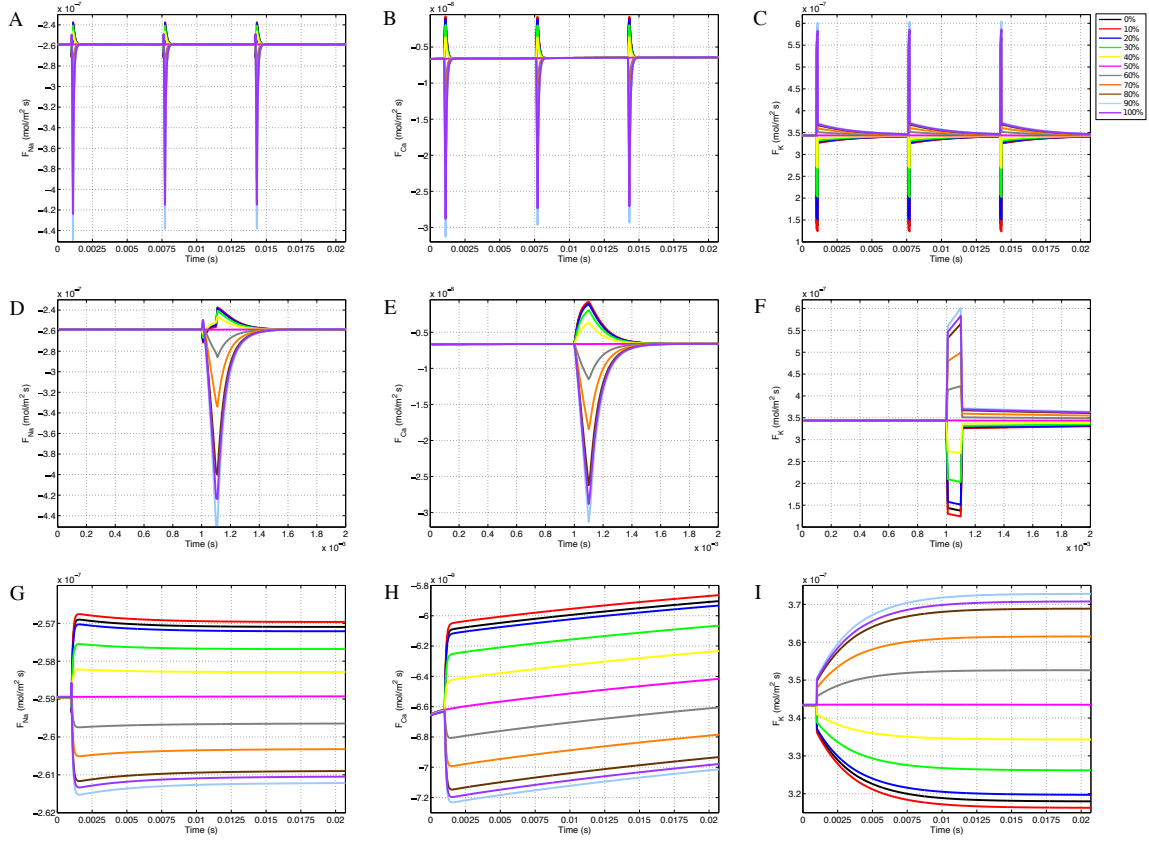


Figure 15: **Transmembrane ionic flux during DBS and TES simulations.** A-C: Membrane flux at equispaced locations in the node of Ranvier throughout the whole DBS simulation for sodium (A), calcium (B), and potassium (C). D-F: Flux around the first DBS pulse (first 2 ms of the simulation) for sodium (D), calcium (E), and potassium (F). G-I: Membrane flux during the whole TES simulation for sodium (G), calcium (H), and potassium (I).

increase in calcium influx due to the fact that the neuron becomes depolarized and calcium channel activation (m) increases. In addition, the ranking of these flux curves based on the magnitude of the changes is identical to that of the changes in transmembrane voltage and the gating variable m .

Similarly, Na^+ flux (Figures 15A and D) exhibits the same direction of changes and ranking of change magnitude at each point as observed in Ca^{+2} flux, with the same locations exhibiting increases and decreases in influx. While the direction and magnitude rankings of these changes in flux are comparable, the shape of the Na^+ flux curves are quite different from that of Ca^{+2} . The flux curves for sodium exhibit an initial spike in one direction before continuing in the other direction. While the behavior and shape of the DBS sodium flux curves differs significantly from that of calcium when the pulse is turned on, their curves exhibit similar shapes and time courses when the stimulus is removed and the fluxes return to

their initial value.

Potassium flux (Figures 15C and F) behaves quite differently than both sodium and calcium. Instead of the smooth, gradual changes observed with calcium, potassium's flux curves exhibit a vertical jump immediately when the stimulus is applied at 1 ms (similar to the shape of the transmembrane voltage curves), and then the flux continues to move in the same direction for the remaining 0.1 ms of the DBS pulse, but at a much slower rate than the initial jump. When the pulse is turned off the flux curves display another vertical jump back towards their initial value, but do not quite reach this level. Then, the fluxes move more slowly to return the rest of the way to their initial value. While sodium and calcium flux return back to their initial value 0.05 ms after the stimulus is removed, potassium does not quite return all the way back even after the 6.5 ms break between the pulses. The fact that potassium does not fully recover relates to the fact that the gating variable that governs potassium channels (and thereby flux) is n (Equation 10), which as described in the gating variable section does not completely recover (Figure 13B). On the other hand, m , which regulates both sodium and calcium channels (Equations 9 and 11), recovers quickly so sodium and calcium return back to their initial level at about the same rate because transmembrane voltage and their commanding gating variable also recover by that time.

The behavior of each ion's flux during DBS treatment is clearly different than that of TES treatment. As described above, the DBS-induced flux alterations occur in short pulses of significant changes. On the other hand, with TES the changes in the fluxes are maintained throughout the simulation (Figures 15G-I) because the TES current is applied for the whole time, instead of in short pulses like with DBS. Thus, the changes in transmembrane voltage, gating variables, and flux are sustained throughout for TES while with DBS the alterations occur in an oscillating fashion. While the DBS-induced changes in flux are short-lived, the magnitude is significantly greater than the changes observed in TES. Table 5 shows the maximum flux achieved during TES and DBS as well as the respective percent change in flux at the 90% membrane location to illustrate the difference in the magnitude of changes between TES and DBS. For calcium in particular, influx increases by 369.70% during DBS but only increases by 8.56% during TES. Similarly, sodium influx increases by 73.47% due to DBS while TES only increases sodium influx by 0.99%.

Also, a similar asymmetry as noted in the gating variables is observed in these flux curves as instead of the decreases in sodium and calcium influx on the left side equaling the

Table 5: **Changes in transmembrane flux during neurostimulation treatments.**

	Initial	Deep Brain Stimulation		Transcranial Electrical Stimulation	
	Flux	Flux	Percent Change	Flux	Percent Change
F_{Na}	$-2.59 \cdot 10^{-7}$	$-4.49 \cdot 10^{-7}$	(73.47%)	$-2.62 \cdot 10^{-7}$	(0.99%)
F_{Ca}	$-6.66 \cdot 10^{-9}$	$-3.13 \cdot 10^{-8}$	(369.70%)	$-7.23 \cdot 10^{-9}$	(8.56%)
F_K	$3.43 \cdot 10^{-7}$	$6.01 \cdot 10^{-7}$	(75.02%)	$3.73 \cdot 10^{-7}$	(8.55%)

Table notes: Sodium, calcium, and potassium flux at the 90% membrane location before the neurostimulation application as well as the maximum fluxes achieved during both DBS and TES simulations. The number in the parenthesis shows the percent increase in flux.

increases at the associated location on the right (such as 10% and 90%), with DBS the increases in influx significantly exceed the decreases. Thus, it is clear that DBS causes a larger influx of sodium and calcium into the intracellular space. Despite the fact that the increase in calcium flux during the DBS pulse is significantly larger, since it is only for a brief time the increase in intracellular calcium concentration throughout the simulation is roughly equal for both TES and DBS with increases of 66.39% and 66.84% respectively. Thus, the two treatments seem to have similar effects on overall calcium concentration despite the differences in the shape, time course, and magnitude of changes in calcium flux.

Despite these clear difference in the behaviors of the flux there are some notable similarities. First, the direction of the flux changes are the same at each location. For example, each location where an ion type experiences an increased influx with TES also undergoes an increased influx for that ion with DBS. Another similarity is in the shapes of the curves with the TES sodium flux curve (Figure 15G) also exhibiting an initial spike in the opposite direction as observed with DBS sodium flux (Figure 15A and D). Potassium's flux curves also reveal a comparable shape with a similar vertical change at the start of treatment with TES (Figure 15I) as described with DBS (Figure 15C and F). Also, the order of the curves are the same suggesting that the locations that experience the largest (and smallest) flux alterations are the same with TES and DBS, namely 90% being the location with the largest sodium and calcium influx as well as the largest potassium efflux in both TES and DBS treatments. These similarities suggest connections between the effects of these treatments as well as the biological behavior of the ion channels and fluxes no matter the external conditions.

5 Discussion

Despite successful clinical experiments demonstrating the success of neurostimulation treatments in relieving symptoms of neurodegenerative disorders, it remains elusive exactly how they do so. Mathematical modeling and computer-based simulation has shown to be a valuable component in enhancing neurostimulation efficacy as well as providing an instrument for helping the research community learn about the mechanisms by which it operates. While both *in silico* and biological experimentation have facilitated a greater understanding of neuromodulation, the cellular-level electrodynamics during electrical stimulation treatments still remain highly elusive.

To help address this contention, we have presented a novel mathematical model of two types of neurostimulation that incorporates transmembrane voltage, ion channel gating, individual ion species, and transmembrane ionic flux during treatment to suggest an explanation of how, where, and when cellular-level changes occur during treatment. Experimentally it is difficult to assess these quantities under these conditions (the application of an external current) so mathematical modeling can be advantageous in providing clues into how these treatments work. Thus, with the model and simulations presented in this paper we hope to suggest possible mechanisms by which these treatments operate to suggest directions for future studies, indicate ways to improve this treatment, and/or identify new potential pharmaceutical targets.

A key finding of this work is the location specificity exhibited by the cell's electrical processes due to the application of a TES or DBS current. In particular, results show that these treatments polarize the neuron as expected, however, the degree of voltage change is dependent on the location within a node of Ranvier, a phenomena reported by the deep brain stimulation modeling community [37,38]. In turn, results show that the states of the ion channels also exhibit location-dependent changes, which directly impacts membrane flux and subsequent intracellular sodium, potassium, calcium, and chloride concentrations. While the degree and type of electrical polarization is location dependent, these results show that these treatments effectively elevate resting membrane potential so that ultimately neuron firing is more achievable [32].

Our simulations suggest two possible mechanisms by which neurostimulation operates to relieve disease symptoms. First, the instantaneous polarization of the cell membrane due to

the stimulus application raises the neuron’s resting potential closer to the threshold for firing an action potential in certain regions of the membrane. Thus, one plausible way that neurostimulation helps improve the symptoms of neurodegenerative disorders is by facilitating action potential generation. Our findings also show that the depolarization and changes in ion channel gating due to DBS causes an increase in calcium influx of up to 369.70%, which indicates that during each DBS pulse there is an increase in the concentration of calcium inside the neuron. An increase in calcium influx is also demonstrated in our models of TES, however with TES the increase in flux is smaller but is sustained for a longer period of time versus the high magnitude and short-lived increase with DBS. It is well-known that cytosolic calcium is a key element in the intracellular signaling cascade that enables neurotransmitter secretion as well as cell viability. In addition, a disruption to calcium homeostasis is correlated with neurodegenerative disease [46–49]. Our results augment these findings by showing that TES and DBS directly alter calcium membrane flux and intracellular calcium concentration via voltage gated calcium channels, by 66% over the course of the simulation. These findings may suggest that a possible mechanism by which neurostimulation achieves therapeutic success, in addition to depolarizing the cell, is by altering calcium dyshomeostasis in diseased neurons.

To our knowledge, this model is also the first to simulate two distinct neurostimulation treatments (namely transcranial electrical stimulation and deep brain stimulation) using the same approach, allowing for the cellular effects of these two treatments to be compared directly for the first time. The main difference between these treatments, as shown in our simulation results, is the magnitude and duration of the changes to neuronal electrodynamics. With TES the changes are smaller and persist throughout the whole treatment, but with DBS most alterations are significantly larger and occur in short pulses. While both TES and DBS are effective in relieving symptoms of neurodegenerative disorders, they are typically used for patients in different stages. TES is typically used in earlier stages because the treatment is less invasive. Our simulations show that TES causes smaller changes in transmembrane voltage and flux than DBS, but presumably larger changes are not necessary for early stage patients because the disease has not yet progressed as far, so the small but sustained changes are enough to improve symptoms. On the other hand, DBS is typically administered in later stages, which is justified by these simulation results showing the much larger changes in transmembrane voltage, the gating variable m , and ionic flux during DBS pulses.

5.1 Future Directions

By implementing the simulation software using an object-oriented approach, its utility can be seamlessly extended to other computational studies and future work. Using these tools, we have begun investigating the impact of TES on more biologically complex domains, including one that encompasses three nodes of Ranvier (Figure 16). In addition, we are starting to examine the effect of TES on three-dimensional domains (Figure 17). Finally, we are interested in examining the effects of ionic flux and cytosolic ion concentrations on intracellular signaling pathways that have implications to neurodegenerative disorders.

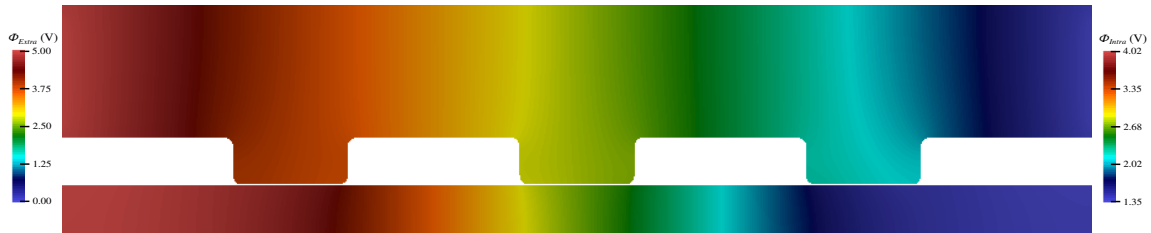


Figure 16: **Electric potential energy throughout a computational domain of a neuron with three nodes of Ranvier.**

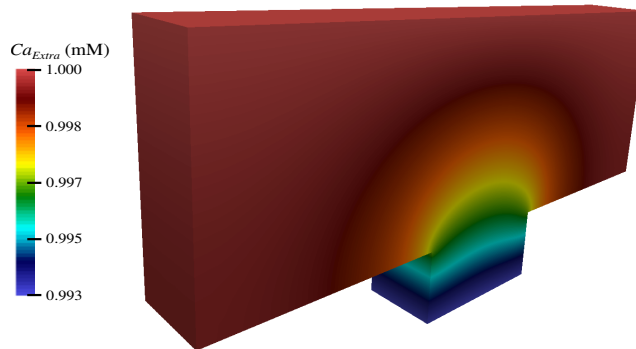


Figure 17: **Extracellular concentration of calcium during TES in a three-dimensional computational domain.**

References

- [1] D. H. Benninger, M. Lomarev, G. Lopez, E. M. Wassermann, X. Li, E. Considine, and M. Hallett. Transcranial direct current stimulation for the treatment of Parkinson’s disease. *J. Neurol. Neurosurg. Psychiatr.*, 81(10):1105–1111, Oct 2010.
- [2] P. S. Boggio, R. Ferrucci, S. P. Rigonatti, P. Covre, M. Nitsche, A. Pascual-Leone, and F. Fregni. Effects of transcranial direct current stimulation on working memory in patients with Parkinson’s disease. *J. Neurol. Sci.*, 249(1):31–38, Nov 2006.
- [3] P. S. Boggio, L. P. Khoury, D. C. Martins, O. E. Martins, E. C. de Macedo, and F. Fregni. Temporal cortex direct current stimulation enhances performance on a visual recognition memory task in Alzheimer disease. *J. Neurol. Neurosurg. Psychiatr.*, 80(4):444–447, Apr 2009.
- [4] P. S. Boggio, C. A. Valasek, C. Campanha, A. C. Giglio, N. I. Baptista, O. M. Lapenta, and F. Fregni. Non-invasive brain stimulation to assess and modulate neuroplasticity in Alzheimer’s disease. *Neuropsychol Rehabil*, 21(5):703–716, Oct 2011.
- [5] A. Antal and W. Paulus. Transcranial alternating current stimulation (tACS). *Front Hum Neurosci*, 7:317, 2013.
- [6] Walter Paulus. Transcranial electrical stimulation (tes tdc; trns, tacs) methods. *Neuropsychological Rehabilitation*, 21(5):602–617, 2011.
- [7] E. M. Caparelli-Daquer, T. J. Zimmermann, E. Mooshagian, L. C. Parra, J. K. Rice, A. Datta, M. Bikson, and E. M. Wassermann. A pilot study on effects of 4 x 1 high-definition tDCS on motor cortex excitability. *Conf Proc IEEE Eng Med Biol Soc*, 2012:735–738, 2012.
- [8] J. J. Borckardt, M. Bikson, H. Frohman, S. T. Reeves, A. Datta, V. Bansal, A. Madan, K. Barth, and M. S. George. A pilot study of the tolerability and effects of high-definition transcranial direct current stimulation (HD-tDCS) on pain perception. *J Pain*, 13(2):112–120, Feb 2012.
- [9] Kelvin L. Chou, Susan Grube, and Parag G. Patil. *Deep brain stimulation : a new life for people with Parkinson’s, dystonia and essential tremor*. Demos Health, 2011.
- [10] Erlick Pereira, Alexander L Green, Dipankar Nandi, and Tipu Z Aziz. Deep brain stimulation: Indications and evidence. *Expert review of medical devices*, 4:591–603, 10 2007.
- [11] M. D. Johnson, S. Miocinovic, C. C. McIntyre, and J. L. Vitek. Mechanisms and targets of deep brain stimulation in movement disorders. *Neurotherapeutics*, 5(2):294–308, Apr 2008.
- [12] Jie Wang, Dongyu Wu, Yan Chen, Ying Yuan, and Meikui Zhang. Effects of transcranial direct current stimulation on language improvement and cortical activation in nonfluent variant primary progressive aphasia. *Neuroscience Letters*, 549:29 – 33, 2013.
- [13] Kyongsik Yun, In-Uk Song, and Yong-An Chung. Changes in cerebral glucose metabolism after 3 weeks of noninvasive electrical stimulation of mild cognitive impairment patients. *Alzheimer’s Research & Therapy*, 8(1):49, Dec 2016.
- [14] Benjamin M. Hampstead, Emily Briceo, Nathan Mascaro, Andoni Mourdoukoutas, and Marom Bikson. Current status of transcranial direct current stimulation in posttraumatic stress and other anxiety disorders. *Current Behavioral Neuroscience Reports*, 3, 03 2016.

- [15] B.M. Hampstead, S Garcia, S Schlaefflin, Katherine Porter, E.R. Smith, B Martis, and S Peltier. Hd-tdcs for combat related ptsd: A case series. *Brain Stimulation*, 10:514, 03 2017.
- [16] Mascha Wout, Sharon M. Longo, Madhavi Reddy, Noah Philip, Marguerite T. Bowker, and Benjamin Greenberg. Transcranial direct current stimulation may modulate extinction memory in posttraumatic stress disorder. *Brain and Behavior*, 7:e00681, 04 2017.
- [17] J D Putzke, R J Uitti, A A Obwegeser, Z K Wszolek, and R E Wharen. Bilateral thalamic deep brain stimulation: midline tremor control. *Journal of Neurology, Neurosurgery & Psychiatry*, 76(5):684–690, 2005.
- [18] Rajesh Pahwa, Kelly E. Lyons, Steven B. Wilkinson, Richard K. Simpson, William G. Ondo, Daniel Tarsy, Thorkild Norregaard, Jean P. Hubble, Donald A. Smith, Robert A. Hauser, and Joseph Jankovic. Long-term evaluation of deep brain stimulation of the thalamus. *Journal of Neurosurgery*, 104(4):506–512, 2006.
- [19] Alim Louis Benabid, Pierre Pollak, Dongming Gao, Dominique Hoffmann, Patricia Limousin, Emmanuel Gay, Isabelle Payen, and Abdhelhamid Benazzouz. Chronic electrical stimulation of the ventralis intermedius nucleus of the thalamus as a treatment of movement disorders. *Journal of Neurosurgery*, 84(2):203–214, 1996.
- [20] Philippe Damier, Stphane Thobois, Tatiana Witjas, Emmanuel Cuny, Philippe-Pierre Derost, Sylvie Raoul, Patrick Mertens, Jean Peragut, Jean-Jacques Lemaire, Pierre Burbaud, Jean-michel Nguyen, P.-M Llorca, and Olivier Rascol. Bilateral deep brain stimulation of the globus pallidus to treat tardive dyskinesia. *Archives of general psychiatry*, 64:170–6, 03 2007.
- [21] Lisbeth Schjerling, Lena Hjermind, Bo Jespersen, Flemming F Madsen, Jannick Brennum, Steen R Jensen, Annemette Lkkegaard, and Merete Karlsborg. A randomized double-blind crossover trial comparing subthalamic and pallidal deep brain stimulation for dystonia clinical article. *Journal of neurosurgery*, 119, 10 2013.
- [22] Donald A. Malone, Darin D. Dougherty, Ali R. Rezai, Linda L. Carpenter, Gerhard M. Friehs, Emad N. Eskandar, Scott L. Rauch, Steven A. Rasmussen, Andre G. Machado, Cynthia S. Kubu, Audrey R. Tyrka, Lawrence H. Price, Paul H. Stypulkowski, Jonathon E. Giftakis, Mark T. Rise, Paul F. Malloy, Stephen P. Salloway, and Benjamin D. Greenberg. Deep brain stimulation of the ventral capsule/ventral striatum for treatment-resistant depression. *Biological Psychiatry*, 65(4):267 – 275, 2009.
- [23] B D Greenberg, L A Gabriels, D A Malone Jr, A R Rezai, G M Friehs, M S Okun, N A Shapira, K D Foote, P R Cosyns, C S Kubu, P F Malloy, S P Salloway, J E Giftakis, M T Rise, A G Machado, K B Baker, P H Stypulkowski, W K Goodman, S A Rasmussen, and B J Nuttin. Deep brain stimulation of the ventral internal capsule/ventral striatum for obsessive-compulsive disorder: worldwide experience. *Molecular Psychiatry*, 15:64 EP –, 05 2008.
- [24] Dongxin Wang, Xuejun Liu, Bin Zhou, Weiping Kuang, and Tiansheng Guo. Advanced research on deep brain stimulation in treating mental disorders. *Experimental and Therapeutic Medicine*, 15(1):3–12, 01 2018.
- [25] Suman Das, Peter Holland, Maarten A. Frens, and Opher Donchin. Impact of transcranial direct current stimulation (tdcs) on neuronal functions. *Front Neurosci*, 10:550–550, Nov 2016.

- [26] Marom Bikson, Masashi Inoue, Hiroki Akiyama, Jackie K. Deans, John E. Fox, Hiroyoshi Miyakawa, and John G. R. Jefferys. Effects of uniform extracellular dc electric fields on excitability in rat hippocampal slices in vitro. *J Physiol*, 557(Pt 1):175–190, May 2004.
- [27] David Liebetanz, Michael A. Nitsche, Frithjof Tergau, and Walter Paulus. Pharmacological approach to the mechanisms of transcranial dcstimulationinduced aftereffects of human motor cortex excitability. *Brain*, 125(10):2238–2247, 2002.
- [28] Charlotte J. Stagg and Michael A. Nitsche. Physiological basis of transcranial direct current stimulation. *The Neuroscientist*, 17(1):37–53, feb 2011.
- [29] Michael Nitsche, David Liebetanz, Andrea Antal, Nicolas Lang, Frithjof Tergau, and Walter Paulus. Modulation of cortical excitability by weak direct current stimulation-technical, safety and functional aspects. *Supplements to Clinical neurophysiology*, 56:255–76, 02 2003.
- [30] Nadira Islam, Mohammad Aftabuddin, Akiyoshi Moriwaki, Yukio Hattori, and Yasuo Hori. Increase in the calcium level following anodal polarization in the rat brain. *Brain Research*, 684(2):206 – 208, 1995.
- [31] Robert D. Adams, Brinda Gupta, and Amy B. Harkins. Validation of electrical stimulation models: intracellular calcium measurement in three-dimensional scaffolds. *Journal of Neurophysiology*, 118(2):1415–1424, 2017. PMID: 28592688.
- [32] M. A. Nitsche, L. G. Cohen, E. M. Wassermann, A. Priori, N. Lang, A. Antal, W. Paulus, F. Hummel, P. S. Boggio, F. Fregni, and A. Pascual-Leone. Transcranial direct current stimulation: State of the art 2008. *Brain Stimul*, 1(3):206–223, Jul 2008.
- [33] Fabiola Alonso, Dorian Vogel, Johannes Johansson, Karin Wardell, and Simone Hemm. Electric field comparison between microelectrode recording and deep brain stimulation systemsa simulation study. *Brain Sciences*, 8(2), 2018.
- [34] Cameron C. McIntyre and Warren M. Grill. Finite element analysis of the current-density and electric field generated by metal microelectrodes. *Annals of Biomedical Engineering*, 29(3):227–235, Mar 2001.
- [35] Pablo A. Alvarado, Christian A. Tottes-Valencia, Alvaro A. Orozco-Guitierrez, Mauricio A. Alvarez, Genaro Daza-Santacoloma, and Hans Carmona-Villada. Modeling and behavior of the simulation of electric propagation during deep brain stimulation. *DYNA*, 83(198):49–58, Sep 2016.
- [36] Mattias Åström, Ludvic U. Zrinzo, Stephen Tisch, Elina Tripoliti, Marwan I. Hariz, and Karin Wårdell. Method for patient-specific finite element modeling and simulation of deep brain stimulation. *Medical & Biological Engineering & Computing*, 47(1):21–28, Jan 2009.
- [37] Cameron C. McIntyre, Warren M. Grill, David L. Sherman, and Nitish V. Thakor. Cellular effects of deep brain stimulation: Model-based analysis of activation and inhibition. *Journal of Neurophysiology*, 91(4):1457–1469, 2004.
- [38] Cameron C McIntyre, Marc Savasta, Lydia Kerkerian-Le Goff, and Jerrold L Vitek. Uncovering the mechanism(s) of action of deep brain stimulation: activation, inhibition, or both. *Clinical Neurophysiology*, 115(6):1239 – 1248, 2004.
- [39] Cameron C McIntyre, Svjetlana Miocinovic, and Christopher R Butson. Computational analysis of deep brain stimulation. *Expert Review of Medical Devices*, 4(5):615–622, 2007.

- [40] E. Mandonnet and O. Pantz. The role of electrode direction during axonal bipolar electrical stimulation: a bidomain computational model study. *Acta Neurochir (Wien)*, 153(12):2351–2355, Dec 2011.
- [41] R. Sadleir. A Bidomain Model for Neural Tissue. *International Journal of Bioelectromagnetism*, 12(1):2–6, 2010.
- [42] E. Dougherty, J. Turner, and F. Vogel. Multiscale coupling of transcranial direct current stimulation to neuron electrodynamics: Modeling the influence of the transcranial electric field on neuronal depolarization. *Comput Math Methods Med*, 2014:1–14, 2014.
- [43] I. Dione, J. Deteix, T. Briffard, E. Chamberland, and N. Doyon. Improved simulation of electrodiffusion in the node of ranvier by mesh adaptation. *Plos One*, 11(8), 2016.
- [44] J. Pods, J. Schönke, and P. Bastian. Electrodiffusion models of neurons and extracellular space using the poisson-nernst-planck equations—numerical simulation of the intra- and extracellular potential for an axon model. *Biophysical Journal*, 105(1):242–254, 2013.
- [45] A. L. Hodgkin and A. F. Huxley. A quantitative description of membrane current and its application to conduction and excitation in nerve. *J Physiol*, 4:500–544, 1952.
- [46] Ilya Bezprozvanny. Calcium signaling and neurodegenerative diseases. *Trends in Molecular Medicine*, 15(3):89 – 100, 2009.
- [47] Philippe Marambaud, Ute Dreses-Werringloer, and Valérie Vingtdeux. Calcium signaling in neurodegeneration. *Molecular Neurodegeneration*, 4(1):20, May 2009.
- [48] D. James Surmeier, Paul T. Schumacker, Jaime D. Guzman, Ema Ilijic, Ben Yang, and Enrico Zampese. Calcium and parkinson’s disease. *Biochemical and Biophysical Research Communications*, 483(4):1013 – 1019, 2017. SI: Neurodegeneration.
- [49] Tito Cali, Denis Ottolini, and Marisa Brini. Calcium signaling in parkinson’s disease. *Cell and Tissue Research*, 357(2):439–454, Aug 2014.
- [50] Gina E Sosinsky, Thomas J Deerinck, Rocco Greco, Casey H Buitenhuis, Thomas M Bartol, and Mark Ellisman. Development of a model for microphysiological simulations: Small nodes of ranvier from peripheral nerves of mice reconstructed by electron tomography. *Neuroinformatics*, 3:133–62, 02 2005.
- [51] I. Lorena Arancibia-Carcamo, Marc C. Ford, Lee Cossell, Kinji Ishida, Koujiro Tohyama, and David Attwell. Node of ranvier length as a potential regulator of myelinated axon conduction speed. *Elife*, 6:e23329, Jan 2017. 28130923[pmid].
- [52] Kae-Jiun Chang and Matthew N. Rasband. Chapter five - excitable domains of myelinated nerves: Axon initial segments and nodes of ranvier. In Vann Bennett, editor, *Functional Organization of Vertebrate Plasma Membrane*, volume 72 of *Current Topics in Membranes*, pages 159 – 192. Academic Press, 2013.
- [53] Tzyy-Leng Horng, Tai-Chia Lin, Chun Liu, and Bob Eisenberg. Pnp equations with steric effects: A model of ion flow through channels. *The Journal of Physical Chemistry B*, 116(37):11422–11441, 2012.
- [54] The Editors of Encyclopaedia Britannica. Node of ranvier, Apr 2016.
- [55] Ariane Briegel, Davi R. Ortega, Elitza I. Tocheva, Kristin Wuichet, Zhuo Li, Songye Chen, Axel Müller, Cristina V. Iancu, Gavin E. Murphy, Megan J. Dobro, Igor B. Zhulin, and Grant J. Jensen. Universal architecture of bacterial chemoreceptor arrays. *Proceedings of the National Academy of Sciences*, 106(40):17181–17186, 2009.

- [56] C. L. Lopreore, T. M. Bartol, J. S. Coggan, D. X. Keller, G. E. Sosinsky, M. H. Ellisman, and T. J. Sejnowski. Computational modeling of three-dimensional electrodiffusion in biological systems: Application to the node of ranvier. *Biophysical Journal*, 95(6):2624–2635, 2008.
- [57] W.L Maxwell. Nodes of ranvier. In Michael J. Aminoff, , and Robert B. Daroff, editors, *Encyclopedia of the Neurological Sciences (Second Edition)*, pages 601 – 604. Academic Press, Oxford, second edition edition, 2014.
- [58] M Rizzone, M Lanotte, B Bergamasco, A Tavella, E Torre, G Faccani, A Melcarne, and L Lopiano. Deep brain stimulation of the subthalamic nucleus in parkinson’s disease: effects of variation in stimulation parameters. *Journal of Neurology, Neurosurgery & Psychiatry*, 71(2):215–219, 2001.
- [59] E. Moro, R. J.A. Esselink, J. Xie, M. Hommel, A. L. Benabid, and P. Pollak. The impact on parkinson’s disease of electrical parameter settings in stn stimulation. *Neurology*, 59(5):706–713, 2002.
- [60] Pdraig E. O’Suilleabhain, William Frawley, Cole Giller, and Richard B. Dewey. Tremor response to polarity, voltage, pulsewidth and frequency of thalamic stimulation. *Neurology*, 60(5):786–790, 2003.
- [61] A. Datta, X. Zhou, Y. Su, L. C. Parra, and M. Bikson. Validation of finite element model of transcranial electrical stimulation using scalp potentials: implications for clinical dose. *J Neural Eng*, 10(3):036018, Jun 2013.
- [62] P. C. Miranda, M. Lomarev, and M. Hallett. Modeling the current distribution during transcranial direct current stimulation. *Clin Neurophysiol*, 117(7):1623–1629, Jul 2006.
- [63] F. Fregni, P. S. Boggio, M. C. Santos, M. Lima, A. L. Vieira, S. P. Rigonatti, M. T. Silva, E. R. Barbosa, M. A. Nitsche, and A. Pascual-Leone. Noninvasive cortical stimulation with transcranial direct current stimulation in Parkinson’s disease. *Mov. Disord.*, 21(10):1693–1702, Oct 2006.
- [64] A. L. HODGKIN and A. F. HUXLEY. A quantitative description of membrane current and its application to conduction and excitation in nerve. *J Physiol*, 117(4):500–544, Aug 1952. 12991237[pmid].
- [65] H. C. Tuckwell. Quantitative aspects of l-type ca^{2+} currents. *Progress in Neurobiology*, 96(1):1–31, 2012.
- [66] A. R. Kay and R. K. Wong. Calcium current activation kinetics in isolated pyramidal neurones of the ca1 region of the mature guinea-pig hippocampus. *The Journal of Physiology*, 392:603–616, 1987.
- [67] J. Sundnes, G. T. Lines, X. Cai, F. N. Bjorn, K. A. Mardal, and A. Tveito. *Computing the electrical activity in the heart*. Springer, Berlin New York, 2006.
- [68] K. A. Mardal, J. Sundes, H. P. Langtangen, and A. Tveito. Systems of pdes and block preconditioning. In H. P. Langtangen and A. Tveito, editors, *Advanced Topics in Computational Partial Differential Equations:Numerical Methods and Diffpack Programming*, Lecture Notes in Computational Science and Engineering, pages 200–236. Springer Berlin Heidelberg, 2003.
- [69] E Hairer and G. Wanner. *Solving Ordinary Differential Equations II: Stiff and Differential-Algebraic Problems*. Springer, Germany, 1996.

- [70] Alan C. Hindmarsh. Odepack, a systematized collection of ode solvers. *Scientific Computing*, pages 55 – 64, 1983.
- [71] H. P. Langtangen and A. Tveito. *Advanced Topics in Computational Partial Differential Equations: Numerical Methods and Diffpack Programming*. Lecture Notes in Computational Science and Engineering. Springer Berlin Heidelberg, 2003.
- [72] Christophe Geuzaine and Jean-Francois Remacle. Gmsh: A 3-d finite element mesh generator with built-in pre- and post-processing facilities. *International Journal for Numerical Methods in Engineering*, 79(11):1309–1331, 2009.
- [73] Martin S. Alnæs, Jan Blechta, Johan Hake, August Johansson, Benjamin Kehlet, Anders Logg, Chris Richardson, Johannes Ring, Marie E. Rognes, and Garth N. Wells. The fenics project version 1.5. *Archive of Numerical Software*, 3(100), 2015.
- [74] Eric Jones, Travis Oliphant, Pearu Peterson, et al. SciPy: Open source scientific tools for Python, 2001–.
- [75] E. Dougherty and J. Turner. An object-oriented framework for versatile finite element based simulations of neurostimulation. *Journal of Computational Medicine*, 2016:1–15, 2016.
- [76] H. P. Langtangen. *Computational Partial Differential Equations: Numerical Methods and Diffpack Programming*. Texts in Computational Science and Engineering. Springer Berlin Heidelberg, 2003.
- [77] Are Magnus Bruaset and Hans Petter Langtangen. Diffpack: A software environment for rapid prototyping of pde solvers, 1994.
- [78] Carlo Miniussi, Stefano F. Cappa, Leonardo G. Cohen, Agnes Floel, Felipe Fregni, Michael A. Nitsche, Massimiliano Oliveri, Alvaro Pascual-Leone, Walter Paulus, Alberto Priori, and Vincent Walsh. Efficacy of repetitive transcranial magnetic stimulation/transcranial direct current stimulation in cognitive neurorehabilitation. *Brain Stimulation*, 1(4):326 – 336, 2008.
- [79] B Reddy. *Introductory functional analysis : with applications to boundary value problems and finite elements*. Springer, New York, 1998.
- [80] Gerald B. Folland. *Real Analysis: Modern Techniques and Their Applications*. Wiley, 2007.

Appendices

Appendix A Mathematical Concepts and Definitions

Here we present preliminary mathematical concepts, definitions, and numerics utilized throughout this thesis.

A.1 Finite Element Method

Many equations that model real life phenomena in science and engineering, including this neurostimulation model, involve partial differential equation (PDE) that cannot be solved analytically. Complex geometries and boundary conditions make finding the exact solution difficult, if not impossible. In such cases, a numerical method, such as the finite element method (FEM), can be used to find an approximate solution. This method is based on the weak formulation of the original PDE system and its governing boundary conditions. Once constructed, the finite element method recasts this weak formulation to the so called discrete formulation by discretizing the solution function space and the domain.

A fundamental theorem in this process is Green's Theorem [79]. Green's Theorem states the divergence of a vector field within a closed curve is equal to the outward flux of the vector field across the surface of the closed curve, and is properly formulated as follows:

Theorem 1 (Green's Theorem). *For all functions u, v in $C^1(\bar{\Omega})$,*

$$\int_{\Omega} u \frac{\partial v}{\partial x_i} dx = \int_{\partial\Omega} uv\nu_i ds - \int_{\Omega} v \frac{\partial u}{\partial x_i} dx, \quad (20)$$

where ν_i is the i^{th} component of the outward unit normal vector ($\boldsymbol{\nu}$) to the boundary $\partial\Omega$ of a domain Ω . Here, we assume that the boundary is sufficiently smooth, and $C^1(\bar{\Omega})$ is defined to be the set of all continuous functions that have continuous first derivatives on $\Omega \cup \partial\Omega$.

The governing equations for partial differential equations include boundary conditions. The forms of boundary conditions used in this project are defined here.

Definition 1: A *Dirichlet boundary condition* specifies values that a PDE solution take on the domain boundary:

$$u(\vec{x}, t) = f(\vec{x}, t), \quad \vec{x} \in \partial\Omega, \quad t \in \mathbb{R}, \quad (21)$$

where $f(\vec{x}, t)$ is a known real-valued function. The Dirichlet boundary condition is commonly referred to as a *fixed* or *essential* boundary condition.

Definition 2: A *Neumann boundary condition* specifies values that the derivative of a PDE solution takes on the domain boundary:

$$k(\vec{x}, t) \frac{\partial u}{\partial \vec{n}} = k(\vec{x}, t) (\nabla u \cdot \vec{n}) = f(\vec{x}, t), \quad \vec{x} \in \partial\Omega, \quad t \in \mathbb{R}, \quad (22)$$

where $f(\vec{x}, t)$ and $k(\vec{x}, t)$ are known real-valued functions. Due to its seamless integration into a PDE weak formulation, a Neumann boundary condition is commonly referred to as a *natural* boundary condition. A homogeneous Neumann boundary condition states that $u(\vec{x}, t)$ does not change in the direction of the outward normal \vec{n} , thus restricting $u(\vec{x}, t)$ to the boundary Ω as a consequence of restricting the flux of $u(\vec{x}, t)$ to zero.

A.1.1 Function Spaces

To properly recast a partial differential equation into its weak formulation, several function spaces are required. These function spaces are defined here.

Definition 3: The space $L^2(\Omega)$ is the set of square-integrable functions on Ω :

$$L^2(\Omega) := \left\{ u(\vec{x}) : \int_{\Omega} |u(\vec{x})|^2 dx < \infty \right\}. \quad (23)$$

Definition 4: The space $H^1(\Omega)$ is the set of functions that are square-integrable and whose first derivative(s) are square integrable on Ω :

$$H^1(\Omega) := \left\{ u(\vec{x}) : u(\vec{x}) \in L^2(\Omega), \frac{\partial u}{\partial \vec{x}} \in L^2(\Omega) \right\}. \quad (24)$$

Definition 5: The space $H_e^1(\Omega)$ is the set of functions that are in $H^1(\Omega)$ and satisfy the essential boundary condition $u(\vec{x}) = e(\vec{x})$ on $\partial\Omega_e$,

$$H_e^1(\Omega) := \left\{ u(\vec{x}) : u(\vec{x}) \in H^1(\Omega), \text{ and } u(\vec{x}) = e(\vec{x}) \text{ for } \vec{x} \in \partial\Omega_e \right\}. \quad (25)$$

The choice of $L^2(\Omega)$, and subsequently $H^1(\Omega)$, as a solution space for our PDEs is so that integrals in our upcoming weak formulations converge. Theorem 1 states that the product of two functions in $L^2(\Omega)$ is also in $L^2(\Omega)$.

Theorem 2 (Cauchy-Schwartz). *Let Ω be a bounded domain in \mathbb{R}^n . If $u(\mathbf{x}), v(\mathbf{x}) \in L^2(\Omega)$, then*

$$\int_{\Omega} u(\mathbf{x})v(\mathbf{x})dx < \infty.$$

Proof of Theorem 2. The proof of this theorem is a direct result of the Cauchy-Schwartz Inequality [80]. In this context, the Cauchy-Schwartz inequality tells us that

$$\int_{\Omega} u(\mathbf{x})v(\mathbf{x})dx \leq \sqrt{\int_{\Omega} |u(\mathbf{x})|^2 dx} \sqrt{\int_{\Omega} |v(\mathbf{x})|^2 dx}.$$

Since $u(\mathbf{x}), v(\mathbf{x}) \in L_2(\Omega)$, by definition,

$$\int_{\Omega} |u(\mathbf{x})|^2 dx < \infty \text{ and } \int_{\Omega} |v(\mathbf{x})|^2 dx < \infty.$$

It follows that

$$\int_{\Omega} u(\mathbf{x})v(\mathbf{x})dx \leq \sqrt{\int_{\Omega} |u(\mathbf{x})|^2 dx} \sqrt{\int_{\Omega} |v(\mathbf{x})|^2 dx} < \infty.$$

□

A.1.2 Finite Element Method Steps

The following detail the main steps in the finite element method to arrive at the discrete formulation.

1. Construct the variational form using Galerkin's method

First, assume that $f \in L^2(\Omega)$ and $u \in V$. The process of generating the variational problem involves multiplying the PDE by an arbitrary test function, $v \in H_0^1$, and integrating over the domain. Then, Greens theorem (the divergence theorem) is applied to integrate the second derivative terms by parts. Using the divergence theorem reduces the order of the derivatives and facilitates the incorporation of boundary conditions.

2. Identify solution spaces

The solution spaces that the trial function (u) and test function (v) are members of must be defined so that the integrals in the weak formulation exist. Boundary conditions that are enforced on the trial solution are called essential (or Dirichlet) boundary conditions. Essential boundary conditions are imposed on the solution space for the trial function $u \in H_E^1$. Natural (or Neumann) boundary conditions are incorporated into the

weak formulation.

3. Discretize the domain

The finite element method breaks up the complex domain (Ω) into discrete components, called elements. As such, the problem is solved on Ω_h , an approximation of Ω . For one-dimensional problems the domain is broken up into line segments. Similarly, for two-dimension domains triangles or quadrilaterals can be used for the elements while tetrahedral and hexahedral elements are typically used in three-dimensional problems.

4. Approximate the solution space(s) with a polynomial space

In this method the trial function in the PDE, u , can be approximated by a function u_h by using linear combinations of basis functions: $u \approx u_h$ and $u_h = \sum \alpha_i \cdot \phi_i$, where ϕ_i denotes the basis function (which represents v) and α_i denotes the coefficients of the basis functions that are used to approximate u with u_h . In other words, u_h is a linear combination of the basis functions. Thus, using the finite element method turns the problem of solving a partial differential equation into solving a system of linear equations. Since α_i is the height of the function it can also be denoted as u_i the value of the function at each location. From here, the discrete formulation is derived where u_h is $\sum \alpha_i \cdot \phi_i$ and v_h is phi_i . By substituting these into the original problem, the problem is thereby reduced to solving a system of linear equations, $A\vec{u} = \vec{b}$.

A.1.3 One Dimensional Example

Figure 18 shows how this process works using a one-dimensional problem. Each basis function (ϕ_i , represented by the black lines) spans two elements with the center point (x_i) representing the node. Each basis function has a value of one at its respective node and a value of zero at all other nodes (i.e. ϕ_2 has a value of zero at all nodes except x_2 where its value is one). Using linear combinations of the basis functions and coefficients the function u (green line) can be approximated with u_h (red dashed line). This example uses linear basis functions, but it is also possible to use other basis functions such as quadratic or cubic functions.

The example on the left uses uniform elements that are equal sized and evenly spaced. However, in the example on the right the elements are not equally sized and spaced. In particular, the elements are placed closer together in regions where the original function exhibits more variability. By using a greater number of elements and adjusting their spacing

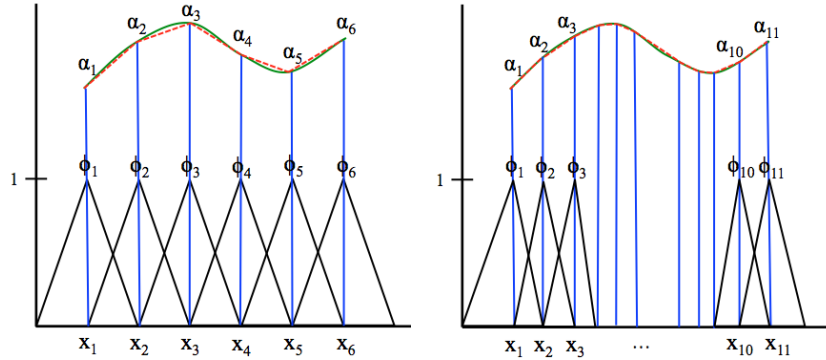


Figure 18: **Illustration of finite element approximation of a one-dimensional problem.**

according to properties of the true solution, the approximation (u_h) is closer to the actual function (u). The finite element method allows for this flexibility in determining how the domain is discretized and selecting the number of elements.

As illustrated above, increasing the number of elements does reduce the error between the true and approximate solution. However, if the domain is larger and/or the equations are being solved multiple times (over multiple time steps), then it could be inefficient or too computationally intensive to continue to increase the number of elements.

A.2 Gauss-Seidel Method

The Gauss-Seidel method is a numerical approach that allows individual equations of a PDE system to be solved independently. This decoupling strategy allows solvers tailored to the individual PDEs to be used and expedites accurate implementation. The Gauss-Seidel method operates according to the following algorithm. We present the Gauss-Seidel method using a system of two differential equations, but the approach could be extended to any number of differential equations.

Let $L_1[u(\vec{x}, t), v(\vec{x}, t)] = f(\vec{x}, t)$ and $L_2[u(\vec{x}, t), v(\vec{x}, t)] = g(\vec{x}, t)$, where $\vec{x} \in \Omega \subset \mathbb{R}^n$, $t \geq 0$. The Gauss-Seidel method decouples this PDE system, solving for u and v independently, but using intermediate solutions in each step of the iterative solution process:

1. Set u and v to initial conditions: $u = u(\vec{x}, 0)$, $v = v(\vec{x}, 0)$.
2. Solve for $u(\vec{x}, t_{n+1})$ using L_1 equation: $L_1[u(\vec{x}, t_{n+1}), v(\vec{x}, t_n)] = f(\vec{x}, t_{n+1})$.
3. Solve for $v(\vec{x}, t_{n+1},)$ using L_2 equation: $L_2[u(\vec{x}, t_{n+1},), v(\vec{x}, t_{n+1},)] = g(\vec{x}, t_{n+1},)$.

This formulation of Gauss-Seidel introduces a global first-order (numerical splitting) error, $O(t)$. Nevertheless, each equation is solved for explicitly and so a small time-step can be used without introducing a significant computational burden.